Inhomogeneous Phases in the Vector Interaction Extended Nambu–Jona-Lasinio Model

Inhomogene Phasen im Nambu–Jona-Lasinio Modell mit Vektorwechselwirkung

Master-Thesis von Marco Schramm

April 2013

TECHNISCHE UNIVERSITÄT DARMSTADT

Fachbereich Physik
Institut für Kernphysik
NHQ

Inhomogeneous Phases in the Vector Interaction Extended Nambu–Jona-Lasinio Model
Inhomogene Phasen im Nambu–Jona-Lasinio Modell mit Vektorwechselwirkung

Vorgelegte Master-Thesis von Marco Schramm

1. Gutachten: PD Dr. Michael Buballa
2. Gutachten: Prof. Dr. Jochen Wambach

Tag der Einreichung:

Abstract

In this thesis we investigate inhomogeneous chiral symmetry breaking phases in the Nambu–Jona-Lasinio model with vector interactions. These are defined by a space-dependent order parameter. We improve the existing ansatz by introducing a space-dependent vector condensate. Inhomogeneous phases are found to be favored in the region of low temperatures and intermediate densities, replacing the phase transition of the homogeneous model up to a certain temperature. We find alterations to previous works concerning the transition from the homogeneous chirally broken phase to the inhomogeneous phase. Furthermore we compare our ansatz of sinusoidal modulations to other possible modulations and find it favored only for lower vector coupling strength.

Zusammenfassung

In dieser Arbeit untersuchen wir inhomogene, die chirale Symmetrie brechende Phasen im Nambu–Jona-Lasinio Modell mit Vektorwechselwirkung. Diese sind definiert über einen ortsabhängigen Ordnungsparameter. Wir verbessern den exitierenden Ansatz, indem wir ein ortsabhängiges Vektor-Kondensat einführen. Wir finden favorisierte inhomogene Phasen bei niedrigen Temperaturen und mittleren Dichten, dort ersetzen sie den Phasenübergang des homogenen Modells bis zu einer bestimmten Temperatur. Unsere Ergebnisse zeigen Unterschiede zu früheren Arbeiten bezüglich des Übergangs von der chiral gebrochenen Phase zur inhomogenen Phase. Weiterhin vergleichen wir unseren Ansatz einer sinusförmigen Modulation mit weiteren Modulationen und stellen fest, dass sie nur im Bereich schwacher Vektorkopplungen favorisiert ist.

Contents

1 Introduction

In the 1950's particle researchers found a number of new particles, their existence remained unexplained at first. The so called 'particle zoo' hinted to a new underlying theory of strong interactions. It was Gell-Mann in 1964 [1] who delivered an explanation, suggesting hadrons consist of quarks. Quantum chromodynamics (QCD) was later introduced in 1973 [2] and is today the most widely accepted theory describing quarks and gluons. The description of the thermodynamics of QCD has made a tremendous progress in recent years and results for high temperatures are available, but some problems still remain. The computing power needed for small quark masses in lattice calculations is enormous and the 'sign problem' [3], lets the method fail for non-vanishing chemical potentials and only recently methods have been developed that allow to go to finite chemical potentials [4]. Although some fixes have been suggested, the ab initio calculations of QCD still fail to describe the low temperature, higher density regime.
The QCD phase diagram is of particular interest. The high temperature, low density regime is accessible through heavy-ion collisions and lattice QCD and evidence for a crossover transition between confined and deconfined matter has been found, for an extensive review see [5]. In the high density, low temperature region a rich phase structure is expected [6]. To investigate this region one has to turn to continuum methods, like Dyson-Schwinger equations [7, 8, 9]. Another possibility is to employ effective models, that feature certain aspects of QCD and are more easily accessible.
The model we want to discuss here is the Nambu–Jona-Lasinio model (NJL model) [10, 11], which shares important symmetries with QCD, one of them the chiral symmetry. We want to use an extended model with a vector interaction term. Investigations in the NJL model have been done quite extensively, see for example [12]. Vector interactions are known to play a crucial role in models similar to NJL, like the Walecka model for nuclear matter [13]. We can extend our model, as the vector interaction term preserves the overall symmetries. In addition it is necessary to describe vector mesons, see for example [14].
We would like to discuss the NJL model in the framework of inhomogeneous condensates, an idea original introduced by Overhauser in 1960 [15] in the context of large static density waves as a ground state of nuclear matter. Still in the 1960's Fulde and Ferrell introduced the possibility of inhomogeneous ground states in superconductors in 1964 [16] and in the same year Larkin and Ovchinnikov discussed this with sinusoidal modulations [17]. Inhomogeneous phases have been found to be important in lower dimensional models, like the $1+1$ dimensional Gross-Neveu model [18], where some important progress has been achieved in the early 2000's and analytical solutions have been found, for example [19, 20, 21]. Later it was shown that the solutions of the lower dimensional models can be transfered to the full NJL model for chiral symmetry breaking phases [22, 23].
In this thesis we want to investigate the properties of the NJL model with vector interactions for inhomogeneous phases. We build up on the work of Stefano Carignano, Dominik Nickel and Michael Buballa presented in [24], where vector interactions have already been discussed. In this paper the approximation was made, that the vector condensate has no explicit modulation. Our goal is to develop a framework where we can allow the vector condensate to have an explicit spatial dependence and calculate the phase diagram and other thermodynamic properties.

Structure of the Document and Conventions

In the second chapter we will develop the general model to investigate inhomogeneous condensates and discuss the special case of a homogeneous order parameter. In the end of that chapter we discuss some aspects of regularization. In chapter 3 we will discuss our results for the homogeneous case and see the influence of vector interactions. The fourth chapter contains some important techniques to enable

numerical calculations and introduce the concrete case of sinusoidal modulations, as well as the gap equations. In chapter 5 we will present our results and compare them to other types of modulations in chapter 6. In the seventh chapter we investigate the competition between two different modulations. We close with summarizing our results and giving an outlook in chapter 8.
Throughout this thesis we use natural units $\hbar = c = 1$, the Einstein sum convention $a^\mu a_\mu = a_0^2 - \sum_{k=1}^3 a_k^2$ and the Feynman slash notation $\not{a} = \gamma^\mu a_\mu$. As a notation of Dirac matrices we use the Weyl representation, unless otherwise stated.

2 Nambu–Jona-Lasinio Model

To examine quark matter in this thesis, we will use the Nambu–Jona-Lasinio model (NJL model) proposed by Nambu and Jona-Lasinio in 1961 [10, 11]. Despite its origins in the pre-QCD era, it has been found to represent some important properties of QCD. It is an effective model that describes strongly interacting fermions via a four-point contact interaction, there are no transmitting particles.

2.1 Lagrangian of the Model

In this work we focus on the two-flavor NJL model extended with an additional term to describe vector interactions. The Lagrangian of the model reads

$$\mathscr{L} = \overline{\psi}\left(i\partial\!\!\!/ - \underline{m}\right)\psi + G_S\left(\left(\overline{\psi}\psi\right)^2 + \left(\overline{\psi}i\gamma_5\tau^a\psi\right)^2\right) - G_V(\overline{\psi}\gamma^\mu\psi)^2. \tag{2.1}$$

Here ψ denotes the quark spinor, $\underline{m} = \mathrm{diag}(m_u, m_d)$ denotes the matrix of up and down bare quark masses, G_S is the scalar coupling constant and G_V is the vector coupling constant. γ are Dirac matrices and τ are Pauli matrices in flavor space. In the following paragraphs we will assume the up and down quark masses to be equal $m_u = m_d = m$.
The first term of the Lagrangian describes free quarks, which are fermionic particles and therefore the Dirac equation is used. In the second term we introduce two interactions, a scalar part and a pseudoscalar part, which have the same coupling constant G_S. The third part describes the vector interaction.

Symmetries

The Lagrangian has different symmetries, that lead to conservation laws via Noether's theorem. It is invariant under global phase transformations $U = \exp(i\alpha)$, $\alpha \in \mathbb{R}$, from which we get baryon conservation. If we assume that the up and down quark masses are equal, we obtain an invariance under rotation in isospin space $U = \exp(-\frac{i}{2}\alpha_a\tau_a)$, which is a $SU_V(2)$ symmetry. If we further demand the quark masses to be zero, we get a third symmetry, which is an axial symmetry $SU_A(2)$, $U = \exp(-\frac{i}{2}\gamma_5\alpha_a\tau_a)$.
The invariance under the combination of the latter two transformations $SU_V(2)\otimes SU_A(2)$ is called chiral symmetry. It is only fulfilled exactly with vanishing bare quark mass, further on we call the case $m = 0$ the chiral limit. For the small finite masses of up and down quark this is an approximate symmetry.

2.2 Mean-Field Approximation

In order to calculate thermodynamic properties we work in a mean-field approximation. We label the expectation values as

$$S(x) = \langle\overline{\psi}\psi\rangle, \tag{2.2}$$
$$P^a(x) = \langle\overline{\psi}i\gamma_5\tau^a\psi\rangle, \tag{2.3}$$
$$n^\mu(x) = \langle\overline{\psi}\gamma^\mu\psi\rangle. \tag{2.4}$$

We expand the condensates around their expectation values

$$\overline{\psi}\psi = S(x) + \delta S, \tag{2.5}$$
$$\overline{\psi}i\gamma_5\tau^a\psi = P^a(x) + \delta P^a, \tag{2.6}$$
$$\overline{\psi}\gamma^\mu\psi = n^\mu(x) + \delta n^\mu \tag{2.7}$$

and assume only small deviations around them. Neglecting quadratic contributions of the δ-terms, the squared condensates read

$$(\overline{\psi}\psi)^2 \approx -S(x)^2 + 2S(x)\overline{\psi}\psi, \tag{2.8}$$

$$(\overline{\psi}i\gamma_5\tau^a\psi)^2 \approx -P^a(x)^2 + 2P_a(x)\overline{\psi}i\gamma_5\tau^a\psi, \tag{2.9}$$

$$(\overline{\psi}\gamma^\mu\psi)^2 \approx -n^\mu(x)^2 + 2n^\mu(x)\overline{\psi}\gamma_\mu\psi. \tag{2.10}$$

The expectation values could in principle still depend on space and time, but we want to focus only on spatially-dependent values. We will only take into account diagonal contributions in flavor space $P_a(\vec{x}) = P(\vec{x})\delta_{a3}$ and time components in the vector condensate $n^\mu(\vec{x}) = n(\vec{x})g^{\mu 0}$. The latter might be questionable for space-dependent condensates, but for the cases relevant in this thesis we can show that the space components vanish (see appendix A).
Using equations (2.8) to (2.10), we arrive at the mean-field Lagrangian

$$\begin{aligned}\mathscr{L}_{MF} = \overline{\psi}\left(i\partial\!\!\!/ - m + 2G_S\left[S(\vec{x}) + i\gamma_5\tau^3 P(\vec{x})\right] - 2\gamma_0 G_V n(\vec{x})\right)\psi \\ - G_S\left(S^2(\vec{x}) + P^2(\vec{x})\right) + G_V n^2(\vec{x}).\end{aligned} \tag{2.11}$$

2.3 Thermodynamic Potential

We want to derive thermodynamic properties of quark matter. In order to do so we calculate the grand potential Ω.
It is well known from statistical mechanics that the thermodynamic potential per volume for a grand canonical ensemble is given by

$$\Omega = -\frac{T}{V}\ln Z, \tag{2.12}$$

with the temperature T, the volume V and the partition function Z.
The partition function is given by [25]

$$Z = \mathrm{Tr}\left[\exp(-\beta(H-\mu Q))\right] \tag{2.13}$$

$$= \int [d\pi]\int [d\psi]\exp\left(\int_0^\beta d\tau\int d^3x\left(\pi\frac{\partial\psi}{\partial\tau} - \left(\mathscr{H}_d - \mu\psi^\dagger\psi\right)\right)\right), \tag{2.14}$$

where $Q = \int d^3x\psi^\dagger\psi$ is the conserved charge from the baryon conservation, $\beta = 1/T$ is the inverse temperature, $\tau = it$ is the imaginary time variable, $\mathscr{H}_d$ is the Hamilton density, μ is the chemical potential and π is the conjugate momentum

$$\pi = \frac{\partial}{\partial(\partial^0\psi)}\mathscr{L} = i\psi^\dagger. \tag{2.15}$$

The Hamiltonian in mean-field approximation can be computed from the Lagrangian and the fields

$$\mathscr{H}_{MF} = \pi\frac{\partial\psi}{\partial t} - \mathscr{L}_{MF} \tag{2.16}$$

$$\begin{aligned}=&\overline{\psi}\left(i\vec{\gamma}\cdot\vec{\nabla} + m - 2G_S\left[S(\vec{x}) + i\gamma_5\tau^3 P(\vec{x})\right] + 2\gamma_0 G_V n(\vec{x})\right)\psi \\ &+ G_S\left(S^2(\vec{x}) + P^2(\vec{x})\right) - G_V n^2(\vec{x})\end{aligned} \tag{2.17}$$

$$=: \overline{\psi}\left(\gamma_0\mathscr{H}\right)\psi - \mathscr{V}_0, \tag{2.18}$$

where we abbreviated the expression in the last step. The partition function can now be expressed as

$$Z = \int [id\psi^\dagger] \int [d\psi] \exp\left(\left\{ \int_0^\beta d\tau \int d^3x \psi^\dagger \left[i\partial_0 - (\mathscr{H} - \mu) \right] \psi \right\} + \mathscr{V} \right), \tag{2.19}$$

where we abridged $\mathscr{V} = \int d\tau \int d^3x \mathscr{V}_0$. At this point it is useful to introduce some definitions that will be clear in a moment

$$M(\vec{x}) = m - 2G_S \left(S(\vec{x}) + iP(\vec{x}) \right), \tag{2.20}$$

$$\tilde{\mu}(\vec{x}) = \mu - 2G_V n(\vec{x}). \tag{2.21}$$

We call $M(\vec{x})$ the shifted mass and $\tilde{\mu}(\vec{x})$ the shifted chemical potential. Now we can write down the Hamiltonian as a direct product of two isospectral Hamiltonians

$$\mathscr{H} - \mu = i\gamma_0 \vec{\gamma} \vec{\partial} + \gamma_0 \frac{1}{2} \left[M(\vec{x}) + M^*(\vec{x}) + \gamma_5 \tau^3 M(\vec{x}) - \gamma_5 \tau^3 M^*(\vec{x}) \right] - \tilde{\mu}(x) \tag{2.22}$$

$$= \left(\mathscr{H}_+ - \mu \right) \otimes \left(\mathscr{H}_- - \mu \right), \tag{2.23}$$

where each new Hamiltonian contains one part of the flavor matrix. Using the Weyl representation for the Dirac structure we arrive at two simple expressions

$$\mathscr{H}_+ - \mu = \begin{pmatrix} -i\vec{\sigma}\vec{\partial} - \tilde{\mu}(\vec{x}) & M(\vec{x}) \\ M^*(\vec{x}) & i\vec{\sigma}\vec{\partial} - \tilde{\mu}(\vec{x}) \end{pmatrix}, \quad \mathscr{H}_- - \mu = \begin{pmatrix} -i\vec{\sigma}\vec{\partial} - \tilde{\mu}(\vec{x}) & M^*(\vec{x}) \\ M(\vec{x}) & i\vec{\sigma}\vec{\partial} - \tilde{\mu}(\vec{x}) \end{pmatrix}. \tag{2.24}$$

Both matrices contribute equally to the thermodynamic potential, which will only result in a factor $N_F = 2$.
In order to calculate the partition function, we perform a Fourier transformation. To transform the shifted mass and chemical potential, we will assume that they are periodical in space

$$M(\vec{x}) = M(\vec{x} + \vec{n}_i), \qquad i = 1, 2, 3, \tag{2.25}$$

with the vectors $\vec{n}_i$ spanning a unit cell. We label the wave number $q_k = (0, \vec{q}_k)$, which equals a reciprocal lattice vector. For the shifted chemical potential, twice the wave number is expected. This has been found for a special case in [24] and we will check this assumption later on in section 6.2. We get a discrete Fourier decomposition

$$M(\vec{x}) = \sum_{\vec{q}_k} M_{\vec{q}_k} e^{i\vec{q}_k \vec{x}}, \tag{2.26}$$

$$\tilde{\mu}(\vec{x}) = \sum_{\vec{q}_k} \tilde{\mu}_{\vec{q}_k} e^{i2\vec{q}_k \vec{x}}. \tag{2.27}$$

We transform the fields as well

$$\psi(\vec{x}, \tau) = \frac{1}{\sqrt{V}} \sum_n \sum_{\vec{p}_m} e^{i(\vec{p}_m \vec{x} + \omega_n \tau)} \widetilde{\psi}_{n, \vec{p}_m}, \tag{2.28}$$

$$\psi^\dagger(\vec{x}, \tau) = \frac{1}{\sqrt{V}} \sum_n \sum_{\vec{p}_m} e^{-i(\vec{p}_m \vec{x} + \omega_n \tau)} \widetilde{\psi}^\dagger_{n, \vec{p}_m}, \tag{2.29}$$

with fermionic Matsubara frequencies

$$\omega_n = (2n + 1)\pi T. \tag{2.30}$$

The fields in the imaginary time formalism are anti periodic in the zero component. For the space components we assume the volume to be spanned by multiples of the unit cell $\sum_{i=1}^{3} N_i \vec{n}_i$ with $N_i \in \mathbb{N}$. The momenta should be periodic in the volume V, so they are discrete following the relation $\vec{p}_m \vec{n}_i = 2\pi N_{m\,i}/N_i$ with $N_{m\,i} \in \mathbb{Z}$. We will take the infinite volume limit later on, so we end up with continuous momenta. From the integration over space and time in the partition function we get Kronecker deltas. The Hamiltonian is not diagonal in momentum space

$$\mathscr{H}_{\vec{p}_m,\vec{p}_{m'}} - \mu = \begin{pmatrix} -\vec{\sigma}\vec{p}_m \delta_{\vec{p}_m,\vec{p}_{m'}} + \sum_{\vec{q}_k} \tilde{\mu}_{\vec{q}_k} \delta_{2\vec{q}_k,(\vec{p}_m - \vec{p}_{m'})} & -\sum_{\vec{q}_k} M_{\vec{q}_k} \delta_{\vec{q}_k,(\vec{p}_m - \vec{p}_{m'})} \\ -\sum_{\vec{q}_k} M_{\vec{q}_k} \delta_{\vec{q}_k,(\vec{p}_{m'} - \vec{p}_m)} & \vec{\sigma}\vec{p}_m \delta_{\vec{p}_m,\vec{p}_{m'}} + \sum_{\vec{q}_k} \tilde{\mu}_{\vec{q}_k} \delta_{2\vec{q}_k,(\vec{p}_m - \vec{p}_{m'})} \end{pmatrix}. \tag{2.31}$$

Instead M and $\tilde{\mu}$ couple two momenta that differ by $\vec{q}_k$ or $2\vec{q}_k$. The partition function reads

$$Z = \prod_n \prod_{\vec{p}_m,\vec{p}_{m'}} \int [id\widetilde{\psi}^{\dagger}_{n,\vec{p}_{m'}}] \int [d\widetilde{\psi}_{n,\vec{p}_m}] \exp\left(\sum_n \sum_{\vec{p}_m,\vec{p}_{m'}} i\widetilde{\psi}^{\dagger}_{n,\vec{p}_{m'}} \beta \left[i\omega_n - (\mathscr{H}_{\vec{p}_{m'},\vec{p}_m} - \mu) \right] \widetilde{\psi}_{n,\vec{p}_m} + \mathscr{V} \right). \tag{2.32}$$

$\widetilde{\psi}^{\dagger}_{n,\vec{p}_{m'}}$ and $\widetilde{\psi}_{n,\vec{p}_m}$ are Grassman fields, so the integration yields

$$Z = \prod_n \det\left(\beta \left[i\omega_n - (\mathscr{H} - \mu) \right]\right) \exp(\mathscr{V}). \tag{2.33}$$

The thermodynamic potential is

$$\Omega = -\frac{T}{V} \ln Z \tag{2.34}$$

$$= -\frac{T}{V} \left\{ \sum_n \ln\det\left(\beta \left[i\omega_n - (\mathscr{H} - \mu) \right]\right) + \mathscr{V} \right\}. \tag{2.35}$$

It is useful to define the condensate part of the grand potential

$$\Omega_{cond} := -\frac{T}{V} \mathscr{V} \tag{2.36}$$

$$= -\frac{T}{V} \left(\int_0^{\beta} d\tau \int d^3x \left[-\frac{|M(\vec{x}) - m|^2}{4G_S} + \frac{(\tilde{\mu}(\vec{x}) - \mu)^2}{4G_V} \right] \right) \tag{2.37}$$

$$= -\frac{1}{V} \int d^3x \left[-\frac{|M(\vec{x}) - m|^2}{4G_S} + \frac{(\tilde{\mu}(\vec{x}) - \mu)^2}{4G_V} \right]. \tag{2.38}$$

Here we used equations (2.20) and (2.21) to express $S(\vec{x})$, $P(\vec{x})$ and $n(\vec{x})$ and the fact that the shifted mass and shifted chemical potential are time independent, so the integration over τ just gives a factor $\beta = 1/T$.
For the remaining, kinetic, part we use the relation $\ln\det D = \mathrm{Tr}\ln D$

$$\Omega_{kin} = -\frac{T}{V} \sum_n \ln\left\{ \det\left(\beta \left[i\omega_n - (\mathscr{H} - \mu) \right]\right) \right\} \tag{2.39}$$

$$= -\frac{T}{V} \sum_n \mathrm{Tr}_{C,\tau,D,\vec{p}} \left\{ \ln\left(\beta \left[i\omega_n - (\mathscr{H} - \mu) \right]\right) \right\} \tag{2.40}$$

$$= -\frac{T}{V} N_C N_F \sum_n \mathrm{Tr}_{D,\vec{p}} \left\{ \ln\left(\beta \left[i\omega_n - (\mathscr{H} - \mu) \right]\right) \right\}, \tag{2.41}$$

where we got constants N_C and N_F from color and flavor space. The trace of a logarithm of a matrix is just the sum over the logarithms of its eigenvalues. We call the eigenvalues of $(\mathscr{H} - \mu)$ in momentum and Dirac space E_λ. We can calculate the sum over the Matsubara frequencies

$$T \sum_n \ln(\beta[i\omega_n - E_\lambda]) = \frac{E_\lambda}{2} + T \ln\left(1 + e^{-E_\lambda/T}\right) = T \ln\left[2\cosh\left(\frac{E_\lambda}{2T}\right)\right] \tag{2.42}$$

and the thermodynamic potential is

$$\Omega = \Omega_{kin} + \Omega_{cond}, \tag{2.43}$$

$$\Omega_{kin} = -N_c N_f \frac{1}{V} \sum_{E_\lambda} T \ln\left[2\cosh\left(\frac{E_\lambda}{2T}\right)\right], \tag{2.44}$$

$$\Omega_{cond} = -\frac{1}{V} \int d^3x \left[-\frac{|M(\vec{x}) - m|^2}{4G_S} + \frac{(\tilde{\mu}(\vec{x}) - \mu)^2}{4G_V}\right]. \tag{2.45}$$

The crucial task here is to determine the eigenvalues of the Hamiltonian. Right now it is a matrix with uncountable infinite dimensions. We will simplify the problem further in chapter 4. Now we want to introduce the simpler case of homogeneous calculations and derive some properties that will be helpful later on.

2.4 Homogeneous Calculations

In the homogeneous case the shifted mass and chemical potential are independent of $\vec{x}$. It is the limit with only the zeroth-order Fourier components. We label those just M and $\tilde{\mu}$ and drop the Fourier indices. The Hamiltonian is diagonal in momentum space and has only Dirac structure. Flavor and color space have trivial structure as before. We can calculate the eigenvalues analytically

$$E_\lambda = \pm\sqrt{p^2 + M^2} - \tilde{\mu} =: \pm E_p - \tilde{\mu} \tag{2.46}$$

and the equation (2.44) transforms to

$$\Omega_{kin} = -2N_F N_C \frac{1}{V} \sum_{s=\pm1} \sum_p \left[\frac{sE_p - \tilde{\mu}}{2} + T \ln\left(1 + \exp\left(-\frac{sE_p - \tilde{\mu}}{T}\right)\right)\right], \tag{2.47}$$

where we used that each eigenvalue is two-fold degenerate. After some straightforward calculations the potential reads

$$\Omega_{kin} = -2\frac{N_F N_C}{V} \sum_p \left[f_{vac}(p) + f_{med}(p)\right], \tag{2.48}$$

$$f_{vac}(p) = E_p, \tag{2.49}$$

$$f_{med}(p) = T \ln\left(1 + \exp\left\{-\frac{E_p - \tilde{\mu}}{T}\right\}\right) + T \ln\left(1 + \exp\left\{-\frac{E_p + \tilde{\mu}}{T}\right\}\right). \tag{2.50}$$

We can take the continuum limit $V \to \infty$ to transform the sum into an integral, integrate the Ω_{cond} part, which just gives a volume contribution that cancels out and write out the full potential

$$\Omega(T, \mu; M, \tilde{\mu}) = \Omega_{kin}(T; M, \tilde{\mu}) + \Omega_{cond}(\mu; M, \tilde{\mu}), \tag{2.51}$$

$$\Omega_{kin}(T; M, \tilde{\mu}) = -2N_F N_C \int \frac{d^3p}{(2\pi)^3} \left[f_{vac}(p; M) + f_{med}(p, T; M, \tilde{\mu})\right], \tag{2.52}$$

$$\Omega_{cond}(\mu; M, \tilde{\mu}) = \frac{(M - m)^2}{4G_S} - \frac{(\tilde{\mu} - \mu)^2}{4G_V}. \tag{2.53}$$

2.4.1 Gap Equations

In order to evaluate the thermodynamic potential derived above, we need to know the values of the shifted mass M and the shifted chemical potential $\tilde{\mu}$. The two parameters have to extremize the potential and therefore have to fulfill a stationary condition

$$\frac{\partial \Omega}{\partial M} = 0, \qquad \frac{\partial \Omega}{\partial \tilde{\mu}} = 0. \tag{2.54}$$

These conditions might have more than one solution, in this case the solution corresponding to the lower thermodynamic potential is favored. The calculation is straight forward and we obtain the equations

$$M = m + 4G_S N_F N_C \int \frac{d^3p}{(2\pi)^3} \left[\frac{M}{E_p} - \frac{M}{E_p} \left(n_+ + n_- \right) \right], \tag{2.55}$$

$$\tilde{\mu} = \mu - 4G_V N_F N_C \int \frac{d^3p}{(2\pi)^3} \left(n_- - n_+ \right), \tag{2.56}$$

with the occupation numbers

$$n_\pm = \left(1 + \exp\left(\frac{E_p \pm \tilde{\mu}}{T} \right) \right)^{-1}. \tag{2.57}$$

These two self-consistent equations will be solved simultaneously using a numerical Newton method.

2.5 Regularization

The integrals in the thermodynamic potential (2.51) are divergent. We discuss the regularization here for the simpler case of the homogeneous model, but the same principle is applied to the inhomogeneous calculations. Due to the four-point contact interaction of the NJL model, it is not renormalizable. Therefore we have to apply a regularization scheme that is suitable for our investigations. In the kinetic part of the thermodynamic potential (2.52) the integral over the vacuum part f_{vac} is divergent, while the integral over the medium part f_{med} is convergent. We only have to take care of the vacuum part.
All regularization schemes apply a cutoff parameter Λ to the divergent parts and this parameter is tuned so that the model reproduces known properties of matter, for example the pion mass and the pion decay constant. Doing this, one also has to fix the coupling constant G_S and the bare quark mass m.
There are different ways to regularize the divergent parts, two will be discussed here briefly. For a more detailed review of regularization schemes we refer to [26].

2.5.1 3-Momentum Cutoff

The momentum integral found in (2.51) is only dependent on the absolute value of the momentum vector $\vec{p}$, therefore we can calculate the integral in spherical coordinates and just get a factor 4π from the angular integration

$$\int \frac{d^3p}{(2\pi)^3} f_{vac}(p) = 4\pi \int_0^\infty \frac{dp_r}{(2\pi)^3} p_r^2 f_{vac}(p_r). \tag{2.58}$$

Now we can apply a cutoff Λ and limit the radial integration to values $p_r \leq \Lambda$

$$4\pi \int_0^\infty \frac{dp_r}{(2\pi)^3} p_r^2 f_{vac}(p_r) \to 4\pi \int_0^\Lambda \frac{dp_r}{(2\pi)^3} p_r^2 f_{vac}(p_r). \tag{2.59}$$

With this cutoff of the radial momentum the integral is finite. This works quite well in the homogeneous case and is often applied. One of the problems with this scheme is that it breaks Lorentz invariance. In the case of the inhomogeneous model, the three momentum cutoff would not only restrict the maximal momentum, but also the maximum number of coupled momenta. This could lead to unwanted artifacts, so we will not use this regularization scheme in this thesis.

2.5.2 Pauli-Villars Regularization

The Pauli-Villars regularization scheme was originally developed by W. Pauli and F. Villars in 1949 [27]. The basic idea is to subtract a function with the same asymptotic behavior as the original function, so that the two cancel out for asymptotic momenta. The number of regulating functions needed depends on the degree of divergence. For our integrals we need at least two regulator functions. In practice we use three additional functions to ensure better convergence

$$\int \frac{d^3p}{(2\pi)^3} f_{vac}(p) \to \int \frac{d^3p}{(2\pi)^3} \sum_{j=0}^{3} c_j \sqrt{f_{vac}^2(p) + j\Lambda^2}, \tag{2.60}$$

with $c_j = 1, -3, 3, -1$. We can see, that in a divergent function $f_{vac}(p)$ the term $j\Lambda^2$ is negligible for large p and the four summands cancel each other out. Another advantage is, that the theory remains Lorentz invariant with this regularization scheme.
In the presence of spatially-dependent densities, we are not able to separate the potential into vacuum and medium part, but have to regularize the complete integrand.

Throughout this thesis we will use the Pauli-Villars regularization scheme, even in the homogeneous part to make the results comparable. If not otherwise stated we use parameters $\Lambda = 757.048$ MeV and a coupling constant $G_S\Lambda^2 = 6.5994$. These parameters are fitted in the chiral limit to a pion decay constant of $f_\pi = 88$ MeV [28] and a vacuum constituent quark mass $M = 300$ MeV. The vector coupling constant G_V will be treated as a free parameter and varied between values of 0 and G_S.

3 Numerical Results for the Homogeneous Case

Before going to the inhomogeneous case, we want to review some aspects of the homogeneous one. Although this has been done quite extensively (see for example [26, 12]), we want to recapitulate some important aspects, that will be relevant for the discussion of inhomogeneous condensates.
For the inhomogeneous phase we want to do all calculations in the chiral limit, because this simplifies the calculations strongly. In order to get a better comparison of the results for the homogeneous and the inhomogeneous case, we will restrict ourselves to the chiral limit in this chapter as well.

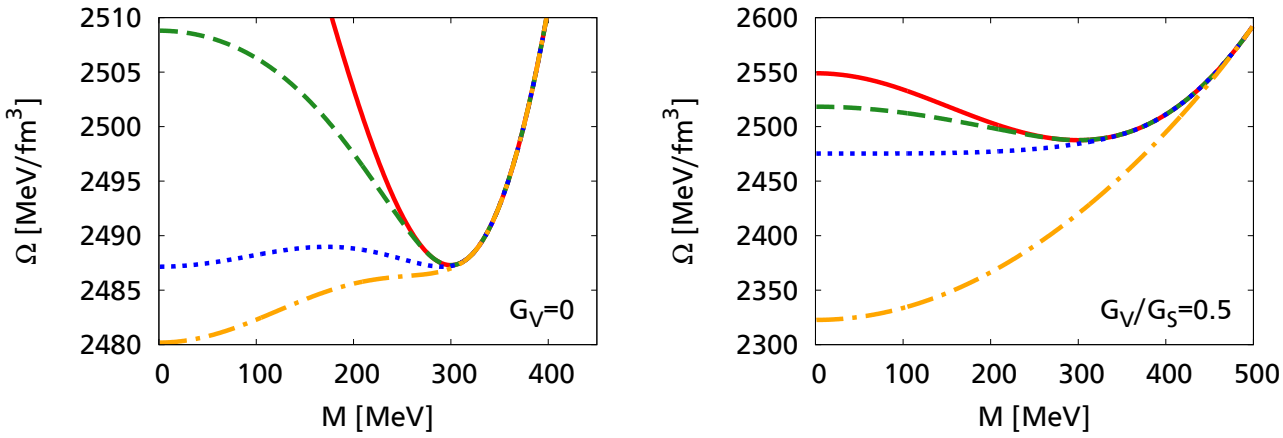

Figure 3.1.: Thermodynamic Potential Ω over effective mass M for various chemical potentials at $T = 1$ MeV and for $G_V = 0$ (left) and $G_V/G_S = 0.5$ with a self-consistent $\tilde{\mu}$ (right). Chemical potenials on the left: 100 MeV (red, solid), 280 MeV (green, dashed), 311.6 MeV (blue, dotted) and 320 MeV (orange, dahsed dotted). Chemical potentials on the right: 100 MeV (red, solid), 280 MeV (green, dashed), 358 MeV (blue, dotted) and 500 MeV (orange, dashed dotted).

3.1 Phase Diagram

On the left side of figure 3.1 the thermodynamic potential as a function of the shifted mass is shown in the absence of vector interactions. Different chemical potentials are used to illustrate the behavior of the shifted mass and the chiral phase transition. In section 2.4.1 we have seen, that the thermodynamic potential has to have an extremum in the mass, and of the multiple possible solutions to the resulting self-consistent equation (2.55), the one corresponding to the lowest thermodynamic potential is favored. For low $\mu = 100$ MeV (red, solid line) we find the favored solution to be $M = 300$ MeV, which we call the vacuum quark mass M_{vac}. At higher chemical potentials $\mu = 280$ MeV (green, dashed line) M_{vac} remains favored. With increasing chemical potential, we see an additional minimum at $M = 0$ MeV, which equals the bare quark mass in the chiral limit. We can find a critical value of $\mu = \mu_c$ (blue, dotted line) where the two minima are degenerate. This point is the chiral phase transition where we have a discontinuous change in the effective quark mass. Further increasing the chemical potential (orange, dashed-dotted line) $M = 0$ becomes the favored solution.
In the right figure, where we allowed for vector interactions, the behavior differs, instead of having two separate minima and a maximum at the critical chemical potential $\mu = 358$ MeV, we only have one very broad minimum (blue, dotted line). The change in the quark mass is therefore continuous, instead of the jump we can see for the case without vector interactions.

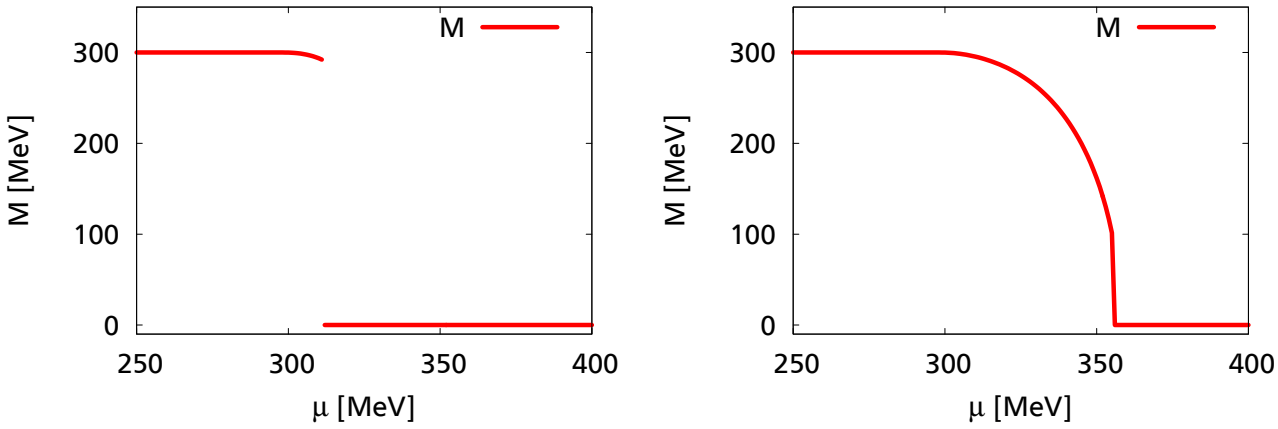

Figure 3.2.: The effective mass as a function of the chemical potential at $T = 1$ MeV for $G_V = 0$ (left) and $G_V/G_S = 0.5$ (right)

If we analyze the self-consistent solutions of the effective mass as a function of the chemical potential (figure 3.2), we can see this behavior in more detail. Below a chemical potential of 300 MeV the mass is constant at a value of $M = M_{vac} = 300$ MeV. For the case without vector interaction we see a slight decrease in the mass before it drops to zero instantly. The discontinuity is exactly where the two minima in figure 3.1 are degenerate. If we allow for vector interactions the continuous decrease of the order parameter happens in a much broader window for μ until the zero axis is reached without any discontinuities. Another thing worth noting is that the transition to the regime where the chiral symmetry is restored, corresponding to a vanishing order parameter ($M = 0$), is shifted to higher chemical potentials. We differentiate two types of transitions from the chirally broken to the chirally restored phase here, a phase transition of first order, where we have discontinuities in the order parameter as seen on the left figure 3.2 and a transition of second order, where the order parameter is continuous, but the first derivative has discontinuities, which is obviously the case in the right figure.
In figure 3.3 we plotted the phase transition lines for different vector coupling constants in the $\mu - T$ plane. In these plots the solid lines indicate first-order transitions, the dots denote their end points and

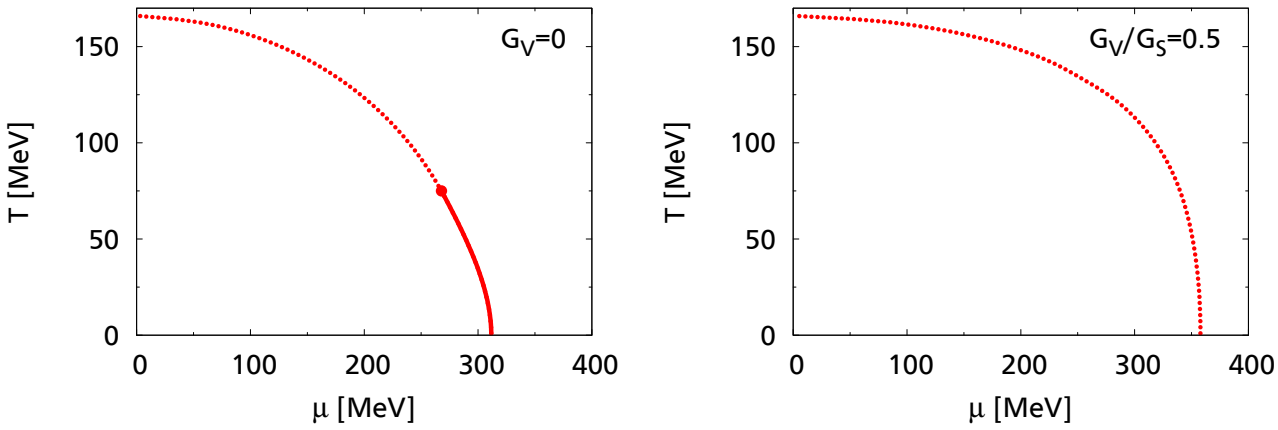

Figure 3.3.: Phase diagram in the μ-T plane for different values of G_V. Solid lines denote first-order phase transitions, dotted lines second-order phase transitions. The critical point is marked with a dot.

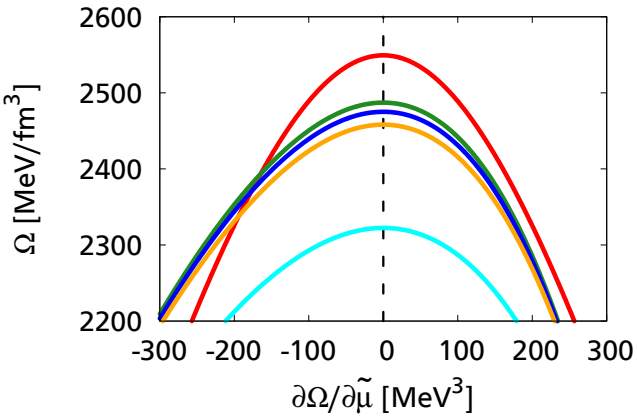

Figure 3.4.: Values of the thermodynamic potential over $\partial\Omega/\partial\tilde{\mu}$ for various chemical potentials (from top to bottom: 1 MeV, 340 MeV, 357.9 MeV, 380 MeV, 500 MeV) at $G_V/G_S = 0.5$ and $T = 1$ MeV.

the dotted lines indicate second-order phase transitions. Left to the phase transition line we are in the chirally broken phase, while right we are in the chirally restored phase. We see immediately, that for higher temperatures the phase transition happens at lower chemical potentials. At a critical temperature $T_c = 166$ MeV the phase transition is at $\mu = 0$ MeV, for higher temperatures no phase transition is present. We can analyze the influence of vector interactions on the phase transition. For $G_V = 0$ we can see the first-order transition up to a temperature of about 75 MeV. For stronger vector coupling this first-order phase transition is shifted to lower temperatures and vanishes completely for coupling constants around $G_V/G_S = 0.5$ and stronger. With increasing G_V the phase transition is shifted to higher chemical potentials, as we have already seen in figure 3.2, but with rising temperatures the phase transition lines approach each other. For vanishing μ the phase transitions for all vector coupling constants happen at the same critical temperature T_c. This is due to the fact, that the self-consistent equation (2.56) only has the solution $\tilde{\mu} = 0$, so there is no dependence on the vector coupling constant anymore.
Another noteworthy point is the behavior of the thermodynamic potential over the shifted chemical potential $\tilde{\mu}$. The repulsive nature of the vector interaction leads to different types of stable solutions of the gap equation. Instead of minimizing the potential, as we have seen for the effective mass, the shifted chemical potential maximizes the energy. We can see in figure 3.4 that the self-consistent solution with $\partial\Omega/\partial\tilde{\mu} = 0$ results in a maximum. This behavior requires a different treatment for inhomogeneous phases than used in most works, we will tackle this in chapter 4.

3.2 Densities

The particle number density n is closely related to the shifted chemical potential $\tilde{\mu}$. It is derived from the average particle number of a grand canonical ensemble

$$\langle N \rangle = T \frac{\partial \ln Z}{\partial \mu}, \tag{3.1}$$

and reads

$$n = \frac{\langle N \rangle}{V} = \frac{T}{V} \frac{\partial \ln Z}{\partial \mu} = -\frac{\partial \Omega}{\partial \mu}. \tag{3.2}$$

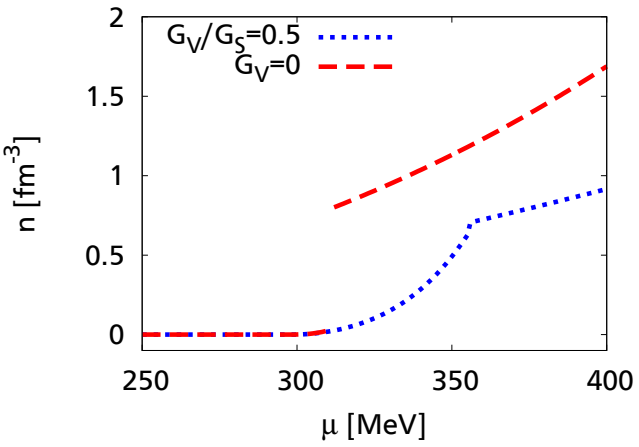

Figure 3.5.: The density n over the chemical potential μ for different vector coupling constants G_V at $T = 1$ MeV.

For the case with vector interactions only the Ω_{cond} part depends on μ explicitly, all implicit dependency vanish because of the gap equations and we get

$$n(\tilde{\mu}) = \frac{\mu - \tilde{\mu}}{2G_V} \tag{3.3}$$

$$= 2N_F N_C \int \frac{d^3p}{(2\pi)^3} \left[-n_+ + n_-\right], \tag{3.4}$$

where we inserted the gap equation in the last step and used the occupation numbers (2.57). For the case without vector interactions equation (3.4) is still true, with $\tilde{\mu} = \mu$. If we look at equation (2.21), we see that the 'condensate' related to the vector interaction term is in fact the density. In figure 3.5 we see the density over chemical potential for different vector couplings. At chemical potentials below the vacuum mass the density is zero, for higher chemical potentials the density starts to rise. The same pattern of discontinuities we have seen in previous plots is present here as well. For weaker coupling strengths, the density jumps to a higher value instantly and grows continuously from there on, while for stronger coupling strengths there is only a discontinuity in the first derivative.

4 Preparations for Numerical Calculations of Inhomogeneous Phases

The Hamiltonian derived in chapter 2 is in general non-diagonal and has uncountable infinite eigenvalues. In order to calculate the thermodynamic potential we need to make some preparations that enable us to tackle this problem.

4.1 Projector

The effective mass and the shifted chemical potential we chose did not have arbitrary modulations, instead we restricted ourselves to static periodical modulations. We have defined the volume as an integer multiple of the unit cell and found that the grid of momenta defined in V is much finer than the unit cell itself (recall: $\vec{p}_m \vec{n}_i = 2\pi N_{mi}/N_i$). This means we can construct each momentum $\vec{p}_m$ by a multiple of the reciprocal lattice vector $\vec{q}_m = \sum_k \lambda_{mk} \vec{q}_k$ with $\lambda_{mk} \in \mathbb{N}$ and a vector in the first Brillouin zone $\vec{k}_m$. The two different momenta of every component of the Hamiltonian $\mathscr{H}$ can be written as

$$\vec{p}_m = \vec{k}_m + \vec{q}_m, \quad \vec{p}_{m'} = \vec{k}_{m'} + \vec{q}_{m'}. \tag{4.1}$$

In the Hamiltonian (2.31) we have seen that only those momenta are coupled by the effective mass and chemical potential that differ by integer multiples of the reciprocal lattice vector $\vec{q}_k$. From this we get the condition $\vec{k}_m = \vec{k}_{m'}$. In addition this means, that the different momenta in the Brillouin zone are decoupled and we can decompose the Hamiltonian in blocks defined by $\vec{k}_m$.
Following [29] we can define a projection

$$\left(P_{\vec{k}_m}\right)_{\vec{p}_m, \vec{p}_{m'}} = \sum_{\vec{q}_m, \vec{q}_{m'} \in R.L.} \delta_{\vec{p}_m - \vec{k}_m, \vec{q}_m} \, \delta_{\vec{p}_{m'} - \vec{k}_m, \vec{q}_{m'}}, \tag{4.2}$$

that projects blocks related to the momentum $\vec{k}_m$ out of the Hamiltonian. We obtain

$$\mathscr{H} = \sum_{\vec{k}_m \in B.Z.} \mathscr{H}(\vec{k}_m) = \sum_{\vec{k}_m \in B.Z.} P_{\vec{k}_m} \mathscr{H}. \tag{4.3}$$

The resulting Hamiltonian $\mathscr{H}(\vec{k}_m)$ has eigenvalues $E_\lambda(\vec{k}_m)$. Inserting this into Equation (2.44) and taking the infinite volume limit leads to

$$\Omega_{kin} = -\frac{N_F N_C}{V} \sum_{\vec{k}_m \in B.Z.} \sum_{E_\lambda} T \ln \left[2 \cosh \left(\frac{E_\lambda(\vec{k}_m)}{2T} \right) \right] \tag{4.4}$$

$$\xrightarrow{V \to \infty} -N_F N_C \int_{B.Z.} \frac{d^3k}{(2\pi)^3} \sum_{E_\lambda} T \ln \left[2 \cosh \left(\frac{E_\lambda(\vec{k})}{2T} \right) \right]. \tag{4.5}$$

4.2 Sinusoidal Ansatz for 1-D Calculations

Now $\mathscr{H}(\vec{k})$ has countable infinite eigenvalues, which is an improvement, but it is still not suitable for a numerical investigation of the problem. In practice we have to apply a cutoff in momentum space. This however does not change the thermodynamic potential dramatically if the cutoff is reasonably large,

since, due to the Pauli-Villars regularization, the influence of large momenta is negligible.
We want to focus on one-dimensional modulations here, so we can express the condensates as

$$M(\vec{x}) = \sum_n M_n e^{in\vec{q}\vec{x}}, \quad \tilde{\mu}(\vec{x}) = \sum_n \tilde{\mu}_n e^{i2n\vec{q}\vec{x}}. \tag{4.6}$$

To write down a concrete matrix for brute-force numerical calculations we start with an ansatz where we only take three Fourier components, -1,0 and +1 for the effective mass and -2, 0 and 2 for the shifted chemical potential. We set $M_{-1} = M_1$ and $\tilde{\mu}_{-1} = \tilde{\mu}_1$ to get real parameters. This results in a sinusoidal modulation

$$M(\vec{x}) = M_0 + M_1 \cos(\vec{q}\vec{x}), \tag{4.7}$$

$$\tilde{\mu}(\vec{x}) = \tilde{\mu}_0 + \tilde{\mu}_1 \cos(2\vec{q}\vec{x}). \tag{4.8}$$

This is a one-dimensional modulation. We can choose the modulation to be in z direction without loss of generality. The other two directions, $\vec{p}_\perp = (p_x, p_y)$, are not limited by the Brillouin zone, but can take all values like in the homogeneous case. We know that the Hamiltonian should only depend on the absolute value of $\vec{p}_\perp$, so it is sufficient to take only the component in x-direction and label it $p_\perp$.
Using the chiral representation of the γ-matrices the Hamiltonian reads

$$\mathscr{H} - \mu = \begin{pmatrix} \ddots & \vdots & \vdots & \vdots & \vdots & \vdots & \iddots \\ \cdots & f_{-m}(k,p_\perp) & \gamma_0\frac{M_1}{2} & -\frac{\tilde{\mu}_1}{2} & 0 & 0 & \cdots \\ \cdots & \gamma_0\frac{M_1}{2} & f_{-(m-1)}(k,p_\perp) & \gamma_0\frac{M_1}{2} & -\frac{\tilde{\mu}_1}{2} & 0 & \cdots \\ \cdots & -\frac{\tilde{\mu}_1}{2} & \gamma_0\frac{M_1}{2} & f_{-(m-2)}(k,p_\perp) & \gamma_0\frac{M_1}{2} & -\frac{\tilde{\mu}_1}{2} & \cdots \\ \cdots & 0 & -\frac{\tilde{\mu}_1}{2} & \gamma_0\frac{M_1}{2} & \ddots & \ddots & \ddots \\ \iddots & \vdots & \vdots & \vdots & \ddots & \ddots & \ddots \end{pmatrix}, \tag{4.9}$$

where each entry equals a 4-by-4 dimensional block in Dirac space, where we abbreviated

$$f_m(k,p_\perp) = \gamma_0\gamma_3(k+mq) + \gamma_0\gamma_1 p_\perp + \gamma_0 M_0 - \tilde{\mu}_0 \tag{4.10}$$

$$= \begin{pmatrix} -(k+mq)-\tilde{\mu}_0 & -p_\perp & M_0 & 0 \\ -p_\perp & (k+mq)-\tilde{\mu}_0 & 0 & M_0 \\ M_0 & 0 & (k+mq)-\tilde{\mu}_0 & p_\perp \\ 0 & M_0 & p_\perp & -(k+mq)-\tilde{\mu}_0 \end{pmatrix}. \tag{4.11}$$

We restrict the modulated momenta to a cutoff Λ_M:

$$|k \pm mq| \leq \Lambda_M, \tag{4.12}$$

therefore the maximal m is

$$m = \lfloor |\Lambda_M - k|/q \rfloor, \tag{4.13}$$

where $\lfloor x \rfloor$ are Gaussian brackets and mean we have to take the greatest integer smaller than x. The size of the matrix has to be quite large to accomplish the necessary precision, but this slows down the overall process extremely. To simplify this and render the problem computable, we use asymptotic eigenvalues described in appendix C. The condensate part of the thermodynamic potential for a one dimensional modulation is

$$\Omega_{cond} = -\frac{1}{L}\int_0^L dz \left[-\frac{|M(z)-m|^2}{4G_S} + \frac{(\tilde{\mu}(z)-\mu)^2}{4G_V} \right], \tag{4.14}$$

with L being the size of the first Brillouin zone, $L = 2\pi/q$. Inserting the sinusoidal ansatz (4.7) and (4.8), the condensate part reads

$$\Omega_{cond} = \frac{1}{4G_S}\left((m-M_0)^2 + \frac{M_1^2}{2} \right) - \frac{1}{4G_V}\left((\mu-\tilde{\mu}_0)^2 + \frac{\tilde{\mu}_1^2}{2} \right). \tag{4.15}$$

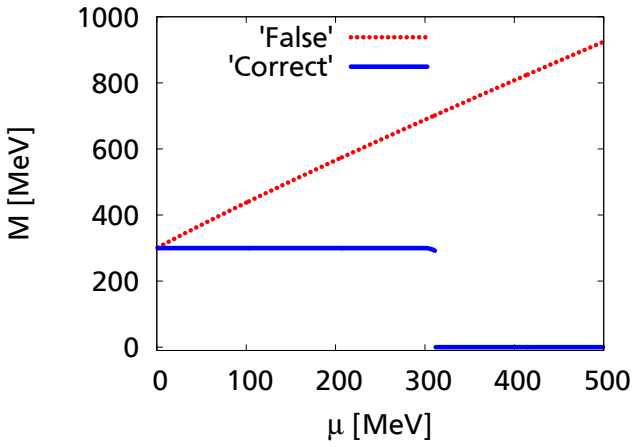

Figure 4.1.: Effective mass as a solution of the gap equation for the homogeneous case over μ, with the chemical potential still in the Pauli-Villars regularized terms (red dotted) and the 'correct' solution (blue solid).

4.3 Regularization

Before we can start calculations by diagonalizing the Hamiltonian, we need to regularize the potential. As already mentioned in section 2.5 we will use the Pauli-Villars regularization scheme. A few additional remarks are necessary to do that.
For our case we cannot split the grand potential into a divergent vacuum and a convergent medium part. Instead we have to regularize the complete kinetic part of the potential. Now one could naively apply this scheme to the eigenvalues E_λ. Here a problem arises. We should not regularize μ, otherwise we find some unwanted artifacts. We can see that already in the homogeneous case, if we apply the regularization the following way $E_p \pm \mu \rightarrow \sqrt{(E_p \pm \mu)^2 + j\Lambda^2}$ we get a rising effective mass with increasing chemical potential, see figure 4.1. Luckily, the chemical potential gives just an offset to the eigenvalues. We can take the zeroth-order Fourier component out of the matrix and define

$$E'_\lambda(k) = E_\lambda(k) - \tilde{\mu}_0. \tag{4.16}$$

In the following we will drop the prime and just use the eigenvalues without $\tilde{\mu}_0$ in the matrix.
Another thing we have to do is introducing a sign function in the hyperbolic cosine of the grand potential. We give an explanation in detail why this is necessary in appendix B.
Applying all methods discussed in the last two sections we find

$$\Omega_{kin} = -N_F N_C \int_{B.Z.} \frac{d^3k}{(2\pi)^3} \sum_{E_\lambda} T \ln\left[2\cosh\left(\frac{E_\lambda(\vec{k})}{2T}\right)\right] \tag{4.17}$$

$$\rightarrow -N_F N_C \int_0^q \frac{dk}{2\pi} \int_0^\infty \frac{dp_\perp}{2\pi} p_\perp \sum_{j=0}^{3} \sum_{E_\lambda} c_j T \ln\left[2\cosh\left(\frac{E_{\lambda,j}(k) - \mathrm{sgn}(E_\lambda)\tilde{\mu}_0}{2T}\right)\right], \tag{4.18}$$

with the eigenvalues now independent of $\tilde{\mu}_0$, sgn() the sign function and

$$E_{\lambda,j}(k) = \sqrt{E_\lambda^2(k) + j\Lambda^2}. \tag{4.19}$$

4.4 Gap Equations

As we have seen in figure 3.4 instead of minimizing the thermodynamic potential, the vector contributions maximize it. So we cannot minimize the thermodynamic potential numerically with respect to the components of $\tilde{\mu}(z)$. Instead we solve the gap equations, which we will derive in this section. We will start with a general approach and then derive them explicitly for our sinusoidal ansatz.
The gap equations take the following form

$$\frac{\partial \Omega}{\partial \tilde{\mu}(z)} = 0, \qquad \frac{\partial \Omega}{\partial M(z)} = 0. \tag{4.20}$$

We want to focus on the gap equations for $\tilde{\mu}(z)$, the other one works analogously. Instead of calculating the gap equation for the complete function $\tilde{\mu}(z)$, we derive one gap equation for every Fourier component. Those have to be identically fulfilled. The zeroth component is straightforward

$$\frac{\partial \Omega}{\partial \tilde{\mu}_0} = -\frac{\tilde{\mu}_0 - \mu}{2G_V} - N_F N_C \int_0^q \frac{dk}{2\pi} \int_0^\infty \frac{dp_\perp}{2\pi} p_\perp \sum_\lambda \sum_{j=0}^{3} c_j \frac{\mathrm{sgn}(E_\lambda)}{2} \tanh\left(\frac{E_{\lambda,j} - \mathrm{sgn}(E_\lambda)\tilde{\mu}_0}{2T}\right). \tag{4.21}$$

For the other components the derivation is somewhat more tricky, the eigenvalues depend on these components, so applying the chain rule we get for $k \neq 0$

$$\begin{aligned} \frac{\partial}{\partial \tilde{\mu}_k} \Omega_{kin} = -N_f N_c \int_0^q \frac{dk}{2\pi} \int_0^\infty \frac{dp_\perp}{2\pi} p_\perp \times \\ \times \sum_{E_\lambda > 0} \sum_j \frac{c_j}{2} \tanh\left(\frac{E_{\lambda,j} - \mathrm{sgn}(E_\lambda)\tilde{\mu}_0}{2T}\right) \left(\frac{E_\lambda}{E_{\lambda,j}} - \tilde{\mu}_0 \delta(E_\lambda)\right) \frac{\partial E_\lambda}{\partial \tilde{\mu}_k}, \end{aligned} \tag{4.22}$$

$$\frac{\partial}{\partial \tilde{\mu}_k} \Omega_{cond} = -\frac{1}{L} \int_0^L \frac{\tilde{\mu}(z) - \mu}{4G_V} \frac{\partial \tilde{\mu}(z)}{\partial \tilde{\mu}_k}. \tag{4.23}$$

To determine the derivatives of the eigenvalues we note that the λ-th eigenvalue can be described as

$$E_\lambda = w_\lambda^\dagger \mathscr{H} w_\lambda, \tag{4.24}$$

where w_λ is the normalized λ-th eigenvector of the Hamiltonian $\mathscr{H}$. Using eigenvalue relations and the hermiticity of the Hamiltonian, one can show that

$$\frac{\partial E_\lambda}{\partial \tilde{\mu}_k} = w_\lambda^\dagger \frac{\partial \mathscr{H}}{\partial \tilde{\mu}_k} w_\lambda \tag{4.25}$$

holds.
To calculate this, we go on to the explicit ansatz.

Sinusoidal Modulation

For the sinusoidal modulation the components of the Hamiltonian look like

$$\begin{aligned} \mathscr{H}_{p,p'} = \gamma_0\gamma_3 p_z \delta_{p,p'} + \gamma_0\gamma_1 p_\perp \delta_{p,p'} + \gamma_0 M_0 \delta_{p,p'} \\ + \gamma_0 \frac{M_1}{2} \delta_{p+q,p'} + \gamma_0 \frac{M_1}{2} \delta_{p,p'+q} - \frac{\tilde{\mu}_1}{2} \delta_{p+2q,p'} - \frac{\tilde{\mu}_1}{2} \delta_{p,p'+2q}. \end{aligned} \tag{4.26}$$

So the derivative is

$$w_\lambda^\dagger \frac{\partial \mathscr{H}}{\partial \tilde{\mu}_1} w_\lambda = \sum_p w_\lambda^\dagger \left[\frac{1}{2} \left(\mathbb{I}_D \delta_{p,p'+2q} + \mathbb{I}_D \delta_{p+2q,p'} \right) \right] w_\lambda \tag{4.27}$$

$$= \sum_p \mathrm{Re} \left[\left(w_\lambda^\dagger \right)_p \left(w_\lambda \right)_{p+2q} \right]. \tag{4.28}$$

where $\left(w_\lambda^\dagger \right)_p \left(w_\lambda \right)_{p+2q}$ indicates we have to multiply the p-th component of the first vector with the $p+2q$-th component of the second one. $\mathbb{I}_D$ is a identity matrix in Dirac space and Re() denotes the real part of the argument, which in the present case of a real symmetric matrix can be dropped, as the eigenvectors are real anyway. We will call this a modified scalar product. Using the definition of $\tilde{\mu}(z)$, the derivatives of the thermodynamic potential read

$$\frac{\partial \Omega_{kin}}{\partial \tilde{\mu}_1} = -N_f N_c \int_0^q \frac{dk}{2\pi} \int_0^\infty \frac{dp_\perp}{2\pi} p_\perp \times \tag{4.29}$$

$$\times \sum_{E_\lambda > 0} \sum_j \frac{c_j}{2} \tanh \left(\frac{E_{\lambda,j} - \mathrm{sgn}(E_\lambda)\tilde{\mu}_0}{2T} \right) \left(\frac{E_\lambda}{E_{\lambda,j}} - \tilde{\mu}_0 \delta(E_\lambda) \right) \left(w_\lambda^\dagger \right)_p \left(w_\lambda \right)_{p+2q},$$

$$\frac{\partial \Omega_{cond}}{\partial \tilde{\mu}_1} = -\frac{1}{2LG_V} \int_0^L dz (\tilde{\mu}_0 + \tilde{\mu}_1 \cos(qz) - \mu) \cos(qz) = -\frac{\tilde{\mu}_1}{4G_V}. \tag{4.30}$$

We derived the self-consistent equations

$$\tilde{\mu}_0 = \mu + 2G_V N_F N_C \int_0^q \frac{dk}{2\pi} \int \frac{dp_\perp}{2\pi} p_\perp \sum_\lambda \sum_{j=0}^3 c_j \frac{\mathrm{sgn}(E_\lambda)}{2} \tanh \left(\frac{E_{\lambda,j} - \mathrm{sgn}(E_\lambda)\tilde{\mu}_0}{2T} \right), \tag{4.31}$$

$$\tilde{\mu}_1 = -4G_V N_F N_C \int_0^q \frac{dk}{2\pi} \int \frac{dp_\perp}{2\pi} p_\perp \times \tag{4.32}$$

$$\times \sum_\lambda \sum_{j=0}^3 \frac{c_j}{2} \tanh \left(\frac{E_{\lambda,j} - \mathrm{sgn}(E_\lambda)\tilde{\mu}_0}{2T} \right) \left(\frac{E_\lambda}{E_{\lambda,j}} - \tilde{\mu}_0 \delta(E_\lambda) \right) \left(w_\lambda^\dagger \right)_p \left(w_\lambda \right)_{p+2q}. \tag{4.33}$$

These equations are solvable and have to be fulfilled. In practice calculating these is numerically very demanding. The modified scalar product for $\tilde{\mu}_1$ consists of a large number of components for large matrices and is not feasible to evaluate to the necessary precision. Instead we will use the method discussed in appendix D.

5 Numerical Results

In this chapter we present the results of the numerical calculations for inhomogeneous condensates with spatially varying shifted chemical potentials. We restrict the discussion to the chiral limit for simplicity. In this limit we can set $M_0 = 0$, which simplifies the calculations. Since we only use one Fourier component of the mass, we label M_1 as M. In this section we want to focus on the sinusoidal modulations of the effective mass and the shifted chemical potential described in the previous chapter.

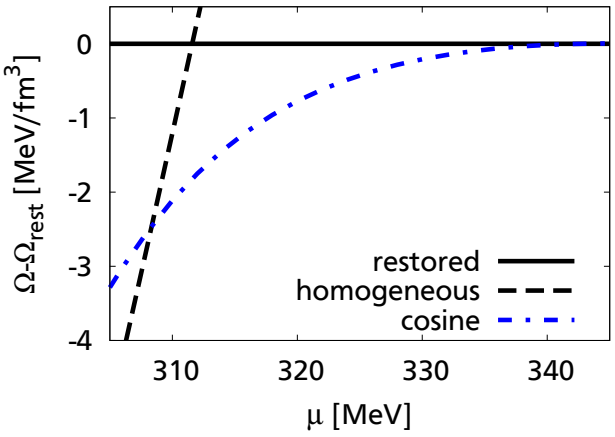

Figure 5.1.: Thermodynamic potential relative to the restored energy for the sinusoidal modulation and the homogeneous case at $T = 1$ MeV and $G_V = 0$.

5.1 Phase Diagram

We can see in figure 5.1 for the case without vector interaction that the sinusoidal ansatz has no continuous limit to the chirally broken homogeneous solutions, instead at a certain chemical potential the homogeneous broken solution becomes favored. This means we have to compare the homogeneous and the inhomogeneous solution and decide which one is favored. In fact the same is true if we allow for vector interactions. The transition to the chirally restored phase on the other hand corresponds to a vanishing mass amplitude.
First of all we would like to focus only on the case without vector interactions and discuss some general properties of inhomogeneous phases. The effective mass $M(z)$ has to minimize the thermodynamic potential, the same way we already saw for homogeneous condensates. Whenever we have multiple possible solutions for the parameters M and q we choose the one with the lowest thermodynamic potential. We can plot the favored solutions in figure 5.2 and see that we have to separate three regions. Below a certain chemical potential $\mu_{crit,1} = 308.25$ MeV the homogeneous solutions are favored, we have an effective mass of about $M = 300$ MeV and a vanishing wave number q, which means we have a non-oscillating solution. At higher chemical potentials we come to the region where the inhomogeneous solutions are favored, we have declining mass amplitude and a rising wave number. There is a first-order transition from the homogeneous chirally broken to the inhomogeneous phase which can easily be understood when we look at figure 5.1 again. The inhomogeneous solutions are not favored in the region $\mu < \mu_{crit,1}$ and the transition is not continuous. The mass amplitude decreases continuously to zero where the chiral symmetry is restored and the wave number becomes irrelevant. This happens at a chemical potential $\mu_{crit,2} = 345$ MeV.

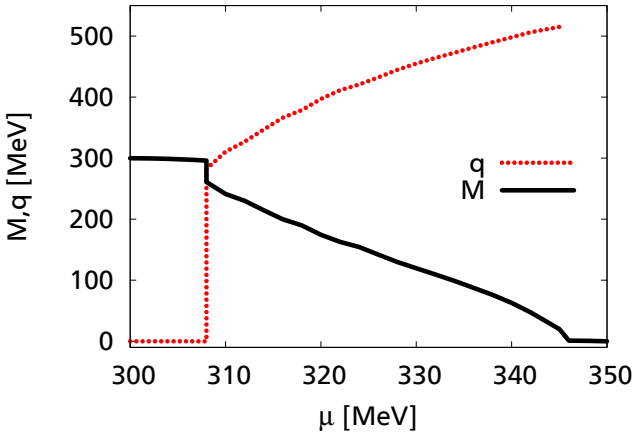

Figure 5.2.: Mass amplitude M and wave number q as a function of chemical potential at $T = 1$ MeV and $G_V = 0$.

Now we can draw a phase diagram for the case without vector coupling in figure 5.3. The blue lines represent the transition from homogeneous chirally broken to the inhomogeneous phase and from the inhomogeneous to the restored phase, for temperatures below the critical point and the transition from the broken to the restored phase above the critical temperature. The red line is the homogeneous phase transition taken from figure 3.3 for comparison. The inhomogeneous phase is favored for temperatures below the critical point, for higher temperatures we only have the transition from the chirally broken to the restored phase. The inhomogeneous phase replaces the homogeneous first-order phase transition completely and the Lifschitz point, the point where the three phase boundaries meet, replaces the critical point we saw in the homogeneous phase diagram[1]. The solid blue line indicates the first-order phase transition from the homogeneous broken to the inhomogeneous phase, while the transition to

[1] Strictly speaking a Lifschitz point is defined as intersection point of three second-order lines. We will use this name here nonetheless to differentiate from the critical point in the homogeneous phase diagram

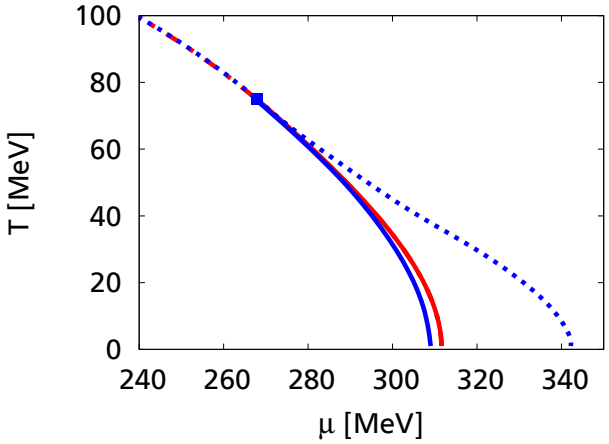

Figure 5.3.: Phase diagram in the $\mu - T$ plane for $G_V = 0$, solid lines indicate first-order phase transitions while dotted lines indicate second-order phase transitions. The blue lines show the phase transitions in the presence of inhomogeneous phases and the red line is the phase transition when limiting to homogeneous condensates.

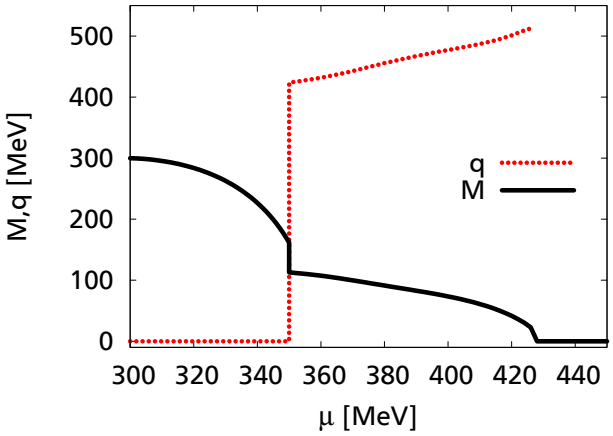

Figure 5.4.: Mass amplitude M and wave number q as a function of chemical potential at $T = 1$ MeV and $G_V/G_S = 0.5$.

the restored phase is always second-order. The first-order transition is an effect of our ansatz for the modulation, if we use a different ansatz, see chapter 6, a second-order transition is possible as well, at least for the case without vector interactions.
If we allow vector interactions the picture remains similar. Here, all our calculations are done with a vector coupling constant $G_V/G_S = 0.5$, unless otherwise stated. In figure 5.4 we show the mass amplitude and wave number. The first-order phase transition from the homogeneous broken to the inhomogeneous phase is still present and the second-order transition to the restored phase as well. Compared to figure 5.2 we see a much longer decline of the mass amplitude in the homogeneous broken regime, which was to be expected, given the behavior seen for the homogeneous solutions in chapter 3. The increase in the wave number is smaller compared to the solutions without vector interaction, where the range was approximately $q \in [300, 500]$, now we only find it to be in the range $q \in [400, 500]$, even though the inhomogeneous phase covers a wider chemical potential range.
This broader μ range covered by the inhomogeneous phase is visible in the phase diagram, figure 5.5,

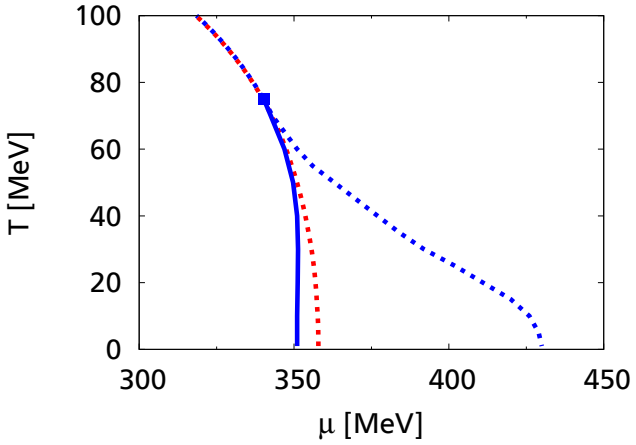

Figure 5.5.: Phase diagram in the $\mu - T$ plane for $G_V/G_S = 0.5$, solid lines indicate first-order phase transition while dotted lines indicate second-order phase transitions. The blue lines show the phase transitions in the presence of inhomogeneous phases and the red line is the phase transition when limiting to homogeneous condensates.

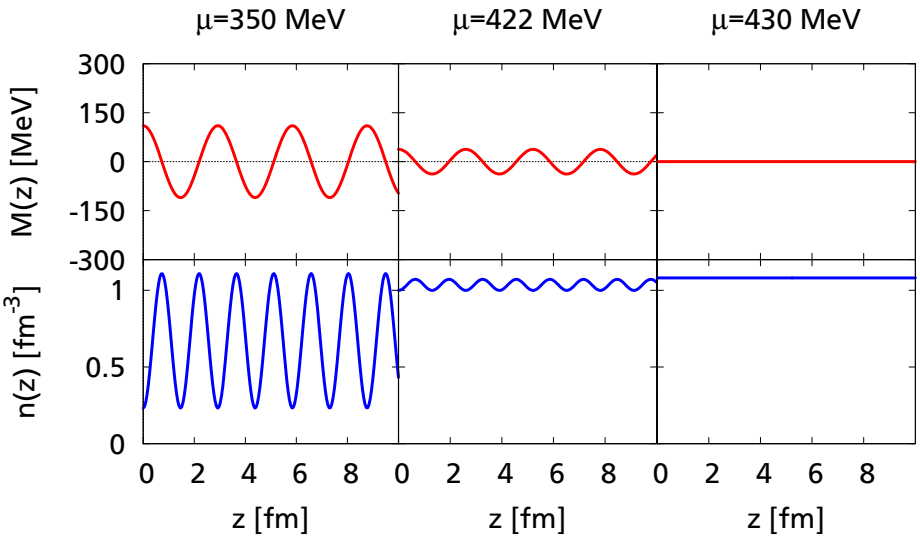

Figure 5.6.: Mass and density profiles for different chemical potentials at $T = 1$ MeV and $G_V/G_S = 0.5$.

as well. As expected from the homogeneous results, the phase transitions are shifted to higher chemical potentials. The first-order transition from the homogeneous broken to the inhomogeneous phase is still present for temperatures below the critical point of the case with $G_V = 0$, as well as the second-order transition to the restored phase. In the case without vector coupling we found the Lifschitz point to be at the same position as the critical point from the homogeneous model, but we already know, that there is no critical point at $G_V/G_S = 0.5$. Nonetheless the Lifschitz point is still present and remains at the same temperature as before, although at a different chemical potential. In fact this is true for all vector coupling strengths, as shown in [24].
In the following we will discuss more detailed the influence of the space-dependent shifted chemical potential in the context of the density.

5.2 Density

The spatial dependent density $n(z)$ is directly related to the shifted chemical potential $\tilde{\mu}(z)$ via equation 2.21. Now we can easily calculate the density

$$n(z) = \frac{\mu - \tilde{\mu}_0}{2G_V} - \frac{\tilde{\mu}_1}{2G_V}\cos(2qz) = \langle n\rangle - n_A\cos(2qz). \tag{5.1}$$

Here we can identify the average density $\langle n\rangle$ and the density amplitude n_A. In figure 5.6 we present the effective mass and the density as a function z for selected chemical potentials. Near the transition to the broken phase at $\mu = 350$ MeV we see an oscillation in the density with a large amplitude around the average value, with a ratio of $n_A/\langle n\rangle = 0.65$. Near the transition to the restored phase at $\mu = 422$ MeV the average value increased, while the amplitude gets smaller, leaving a ratio of just $n_A/\langle n\rangle = 0.035$, until at $\mu = 430$ MeV in the restored phase the density gets constant in space. In this picture we also see that the wave length is half of that of the mass, which was our assumption in chapter 2 that we will test in section 6.2. The wave number of the modulation is increasing with μ, although at a relatively low rate as we already saw in figure 5.4.
The values for $\langle n\rangle$ and the amplitude around it, $\langle n\rangle \pm n_A$, are shown as a function of μ in figure 5.7. In the homogeneous broken regime the density remains constant of course and we see a discontinuity at the first-order transition to the inhomogeneous phase as expected. Here the density starts oscillating

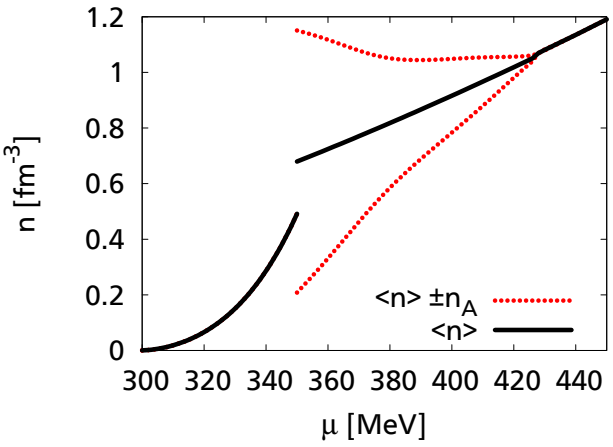

Figure 5.7.: Average density $\langle n \rangle$ (black solid) and the density amplitude n_A (red dotted) at $T = 1$ MeV and $G_V/G_S = 0.5$.

with a large amplitude which continuously declines and vanishes completely in the restored phase. The average density shows a continuous behavior as well.

6 Comparison to Results with Spatially-Constant Shifted Chemical Potential

In this chapter we would like to introduce other possible modulations of the mass functions and their extensions to vector interactions, although for shifted chemical potentials without explicit space dependence.

6.1 Different Types of Modulations

The main focus of this work is on sinusoidal modulation, but we also want to discuss the relation to previous works and different types of modulations. Two of which will be briefly presented here. For a more detailed discussion of the matter we refer for example to [22, 23, 24].

6.1.1 Solitonic Modulations

If we consider only one-dimensional modulations in the NJL model without vector interaction, the Hamiltonian can be mapped on the one of the 1+1 dimensional Gross-Neveu model [22]. For this model an analytical expression for the eigenvalues, as well as for the effective mass are known [21]. We can write the order parameter in terms of Jacobi elliptic functions. In the chiral limit the mass function reads

$$M(z) = \Delta\nu \frac{\mathrm{sn}(\Delta z|\nu)\mathrm{cn}(\Delta z|\nu)}{\mathrm{dn}(\Delta z|\nu)}. \tag{6.1}$$

Here Δ and ν are arbitrary parameters, which we have to tune to self-consistent values. We can however identify the mass amplitude with $M = \Delta\nu$, the period of the modulation with $L = 2\mathbf{K}(\nu)/\Delta$ and the wave number with $q = 2\pi/L$. Here $\mathbf{K}$ is the complete elliptic integral of 1st kind.
To calculate the thermodynamic potential we need the density of states [22]

$$\begin{aligned}\rho_{soliton}(E) = \frac{E\Delta}{\pi^2}\Bigg\{&\theta(\sqrt{\tilde{\nu}}\Delta - E)\left[\mathbf{E}(\tilde{\vartheta}|\tilde{\nu}) + \left(\frac{\mathbf{E}(\nu)}{\mathbf{K}(\nu)} - 1\right)\mathbf{F}(\tilde{\vartheta}|\tilde{\nu})\right] \\ &+ \theta(E - \sqrt{\tilde{\nu}}\Delta)\theta(\Delta - E)\left[\mathbf{E}(\tilde{\nu}) + \left(\frac{\mathbf{E}(\nu)}{\mathbf{K}(\nu)} - 1\right)\mathbf{K}(\tilde{\nu})\right] \\ &+ \theta(E - \Delta)\left[\mathbf{E}(\vartheta|\tilde{\nu}) + \left(\frac{\mathbf{E}(\nu)}{\mathbf{K}(\nu)} - 1\right)\mathbf{F}(\vartheta|\tilde{\nu}) + \frac{\sqrt{(E^2-\Delta^2)(E^2-\tilde{\nu}\Delta^2)}}{E\Delta}\right]\Bigg\}.\end{aligned} \tag{6.2}$$

$\mathbf{F}$ is the incomplete elliptic integral of 1st kind and $\mathbf{E}$ the complete or incomplete integral of 2nd kind. In addition we abbreviated $\tilde{\nu} = 1 - \nu$, $\tilde{\vartheta} = \arcsin(E/(\sqrt{\tilde{\nu}}\Delta))$ and $\vartheta = \arcsin(\Delta/E)$.
The resulting thermodynamic potential reads

$$\Omega(T,\mu;\Delta,\nu) = -N_f N_c \int_0^\infty dE\, \rho_{soliton}(E)\left[f_{vac}(E) + f_{med}(E,T,\mu)\right] + \frac{1}{L}\int_0^L dz\, \frac{|M(z)|^2}{4G_S}, \tag{6.3}$$

with the vacuum and medium part resembling the ones of the homogeneous case from section 2.4

$$f_{vac}(E) = E, \tag{6.4}$$

$$f_{med}(E;T,\mu) = T\ln\left(1 + \exp\left\{-\frac{E-\mu}{T}\right\}\right) + T\ln\left(1 + \exp\left\{-\frac{E+\mu}{T}\right\}\right). \tag{6.5}$$

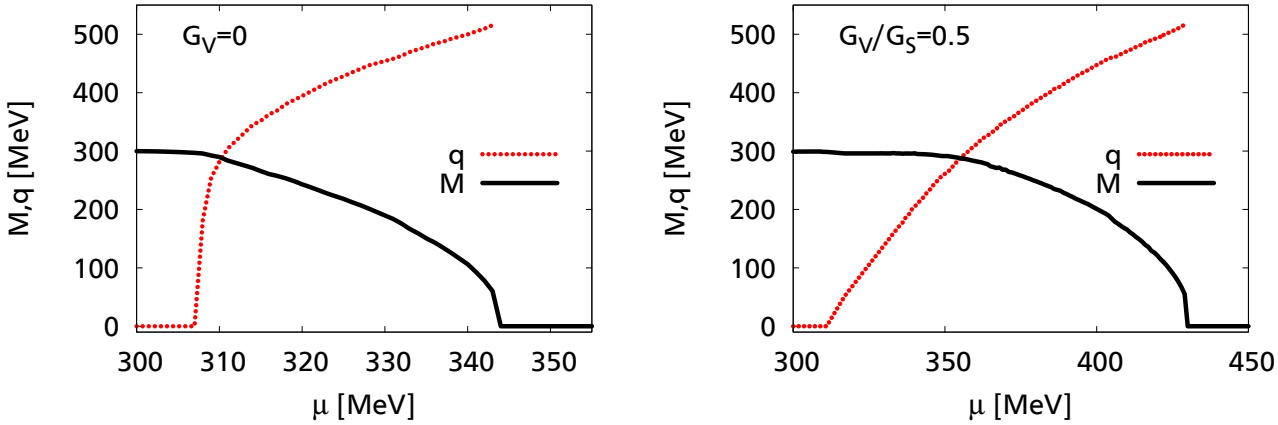

Figure 6.1.: The mass amplitude $M = \Delta\nu$ and the wave number $q = 2\pi\Delta/(2\mathbf{K}(\nu))$ over chemical potential at $G_V/G_S = 0$ (left) and $G_V/G_S = 0.5$ (right) for a solitonic modulation of the mass function at $T = 1$ MeV.

The Pauli-Villars regularization described in 2.5 is applied here.
We can extend this ansatz to vector interactions, if we approximate

$$n(z) \to \bar{n} = \langle n(z) \rangle = \text{const.} \tag{6.6}$$

$$\Rightarrow \tilde{\mu} = \mu - 2G_V\bar{n} = \text{const.} \tag{6.7}$$

Here we sacrifice self-consistency in order to use the analytic solution above. In the following we will sometimes refer to this approximation as spatially-constant densities for brevity. This ansatz has been studied in great detail in [24]. All we have to do is replace μ with $\tilde{\mu}$ in equation (6.5) and extend the thermodynamic potential with an additional condensate part

$$\Omega_{cond,\tilde{\mu}} = -\frac{(\tilde{\mu}-\mu)^2}{4G_V}. \tag{6.8}$$

The mass amplitude and the wave number are shown in figure 6.1 for different vector coupling strengths. For the case without vector interaction the solitons are favored compared to the sinusoidal ansatz and have a continuous limit to the homogeneous chirally broken solutions, resulting in a second-order phase transition from the broken to the inhomogeneous phase.
Another interesting feature of the solitonic modulation is, that for $G_V = 0$ we can calculate density profiles exactly. The resulting space-dependent density reads

$$n_{soliton}(z) = 2N_c \int_0^\infty dE\, \rho_{D,soliton}(E,z)\left(n_-(E) - n_+(E)\right), \tag{6.9}$$

where $n_\pm$ are the occupation numbers and $\rho_{D,soliton}$ is related to the density of states by

$$\rho_{D,soliton}(E,z) = \rho_{soliton}(E)\Big|_{\frac{\mathbf{E}(\nu)}{\mathbf{K}(\nu)} \to -\frac{1}{2}\left(\left(\frac{M(z)}{\Delta}\right)^2 + \nu - 2\right)}. \tag{6.10}$$

The resulting density profiles will act as a test for our case with explicitly modulated shifted chemical potentials. In addition we will compare the phase diagrams of the solitonic solutions with constant densities to the sinusoidal calculations with a modulated density.

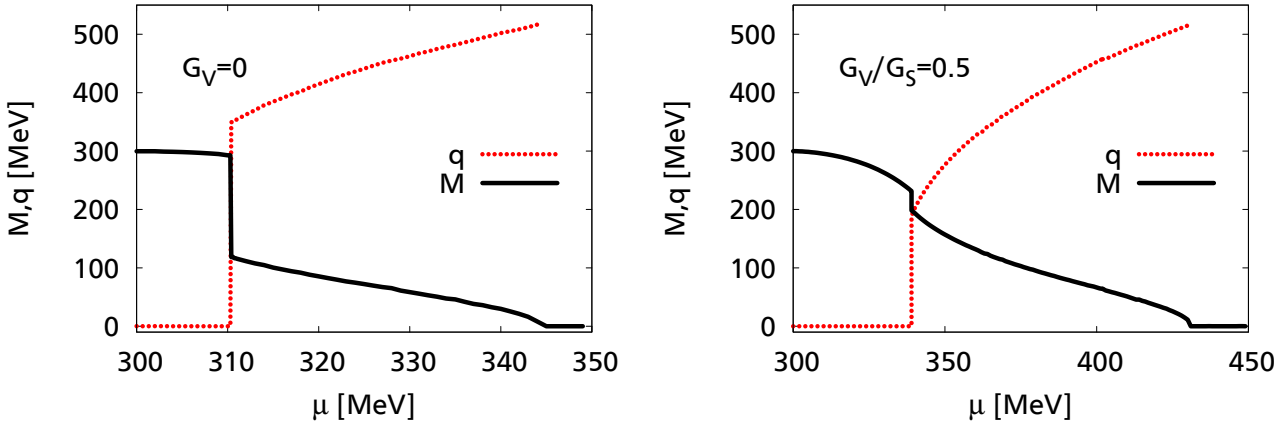

Figure 6.2.: The mass amplitude M and the wave number q over chemical potential at $G_V/G_S = 0$ (left) and $G_V/G_S = 0.5$ (right) for a chiral density wave at $T = 1$ MeV.

6.1.2 Chiral Density Wave

Another possible modulation for the order parameter is the chiral density wave (CDW). It features a complex order parameter given by

$$M_{CDW}(z) = M \exp(iqz). \tag{6.11}$$

Again, we get an analytical expression for the eigenvalues with a density of states

$$\begin{aligned}\rho_{CDW}(E) = \frac{E}{2\pi^2}\Big\{&\theta(E-q-M)\sqrt{(E-q)^2-M^2} \\ &+ \theta(E-q+M)\theta(E+q-M)\sqrt{(E+q)^2-M^2} \\ &+ \theta(q-M-E)\left(\sqrt{(E+q)^2-M^2}-\sqrt{(E-q)^2-M^2}\right)\Big\}.\end{aligned} \tag{6.12}$$

The thermodynamic potential is analogous to equation 6.3 and the extension to vector interactions is performed the same way as for the solitons. For the CDW a spatially constant shifted chemical potential is not an approximation, a density without space dependence is self-consistent. This can be shown by applying a symmetry transformation $\psi \to \exp(i\gamma_5\tau_3 q z_0/2)\psi$ which results in an offset in the mass function, but leaves the density $\langle\psi^\dagger\psi\rangle$ unchanged [24].

6.2 Density Profiles

In chapter 2 one of our first assumptions was to set the wave number of the density to be twice the wave number of the mass. This was motivated from solitonic solutions, discussed in [24], were an analytical solution in the absence of vector interactions is known and an exact density profile can be obtained from equation (6.9) and (6.10). To compare our results to this we have to choose a very weak vector coupling to be closest possible to the results without vector interaction. The presented results in this section are calculated with a coupling constant $G_V/G_S = 0.01$. For this coupling strength we expect the influence of vector interactions on the phase diagram, as well as on the effective mass and wave number to be very small, so the deviation to the results with vanishing vector coupling should be small as well. In figure 6.3 we show density profiles for the solitonic solution at $G_V = 0$ and for the sinusoidal solution at $G_V/G_S = 0.01$. We have chosen a chemical potential not to close to the phase transition to

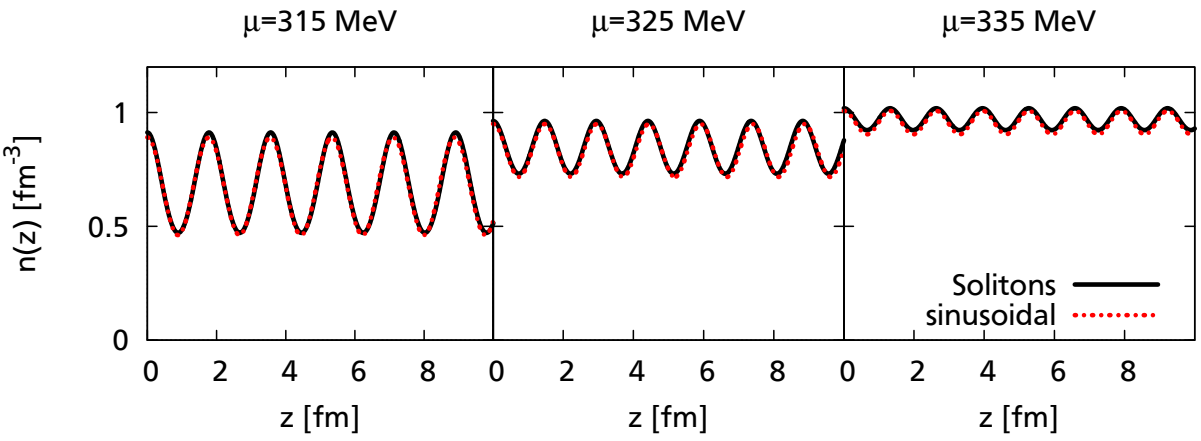

Figure 6.3.: Density profiles for the solitonic modulation at vanishing G_V (black solid) and for the sinusoidal modulation at low coupling strength $G_V/G_S = 0.01$ (red dotted) at $T = 1$ MeV.

the homogeneous chirally broken phase, for those chemical potentials the solitonic modulation equals a sinusoidal shape for better comparison. We see that both modulations are almost indistinguishable. To get a better impression of the difference, we present the relevant parameters in table 6.1. Again we see only minor differences in the parameters, therefore our assumption seems to hold. Some difference is to be expected because of the different modulations used, effects of the vector interaction and of course numerical imprecisions.

	Modulation	q [MeV]	$\langle n \rangle$ [fm^{-3}]	Density Amplitude [fm^{-3}]
$\mu = 315$ MeV	Solitons	347.8	0.68	0.230
	Sinusoidal	348.9	0.67	0.215
$\mu = 325$ MeV	Solitons	421.4	0.85	0.117
	Sinusoidal	418.9	0.83	0.117
$\mu = 335$ MeV	Solitons	470.4	0.97	0.048
	Sinusoidal	469.9	0.96	0.051

Table 6.1.: Wave number, average density and density amplitude for sinusoidal and solitonic modulations and different chemical potentials at $T = 1$ MeV.

6.3 Free Energy Comparison

Comparing the free energies of the three discussed modulations without vector interaction, see figure 6.4 left, we find that the solitonic solution is the most favored, while the sinusoidal is a good approximation with only little difference for almost the complete inhomogeneous phase. Only in the regime close to the homogeneous chirally broken phase, the solitonic solution differs considerably.
If we allow vector interactions now, the picture changes. Comparing the sinusoidal modulation (orange, double dashed) and the solitons (red, double-dotted dashed) both with the approximation of a spatially-constant shifted chemical potential in figure 6.4 (right) it resembles the case without vector interactions. The sinusoidal modulation with explicit space-dependence in $\tilde{\mu}$ on the other hand is disfavored by a huge margin. This raises the question of the validity of approximation (6.7). For the sinusoidal it is certainly not good close to the homogeneous broken phase and we expect the same to be true for the solitons.

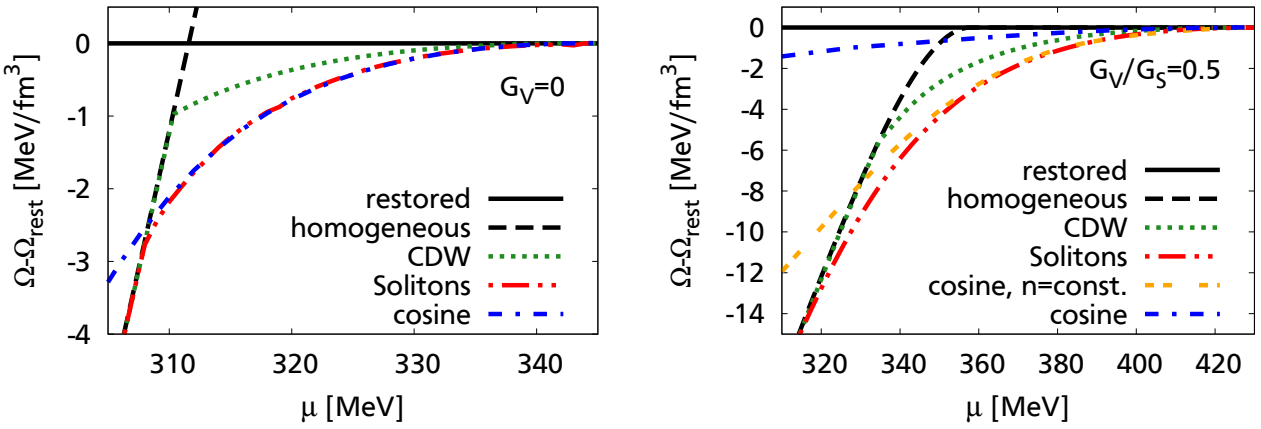

Figure 6.4.: Free energies of different modulations compared to the chirally restored phase at $T = 1$ MeV and $G_V = 0$ (left) and $G_V/G_S = 0.5$ (right).

The chiral density wave is disfavored over the other solutions with constant shifted chemical potentials, but as we already mentioned it can be considered self-consistent with a spatially independent density. It is clearly visible that in the presence of vector interactions and a coupling constant $G_V/G_S = 0.5$ the CDW is favored over the sinusoidal with density modulations. This is an unexpected behavior, we will discuss in chapter 7.

6.4 Phase Diagram

If we compare the phase diagrams in figure 6.5 of the solitonic (black) and the sinusoidal (blue), we see some alterations. The transition from the homogeneous broken to the inhomogeneous phase happens at much lower chemical potentials for solitonic modulations with constant shifted chemical potentials. Additionally the transition is of second-order instead of first, but since the same is true for vanishing vector couplings, this is probably just an artifact of the ansatz. It is obvious that the presence of explicitly modulated shifted chemical potentials changes the picture considerably.
The transition from the inhomogeneous to the restored phase on the other hand seems to be identical for both modulations. Here the assumption of a constant density works quite well, we have seen in figure 5.7 that the density amplitude and therefore the explicit space dependency in the shifted chemical potential decreases towards higher μ and approaches zero near the phase transition. The phase transitions are both second-order, which was to be expected.
The transition from the homogeneous broken phase to the chiral density wave lies between the two other ones. It is of first-order, as expected. The restored phase starts at the same chemical potentials and temperatures as before. We have seen in the previous section, that the CDW is favored over the sinusoidal modulation so for the given vector coupling the inhomogeneous phase is defined by the chiral density wave.

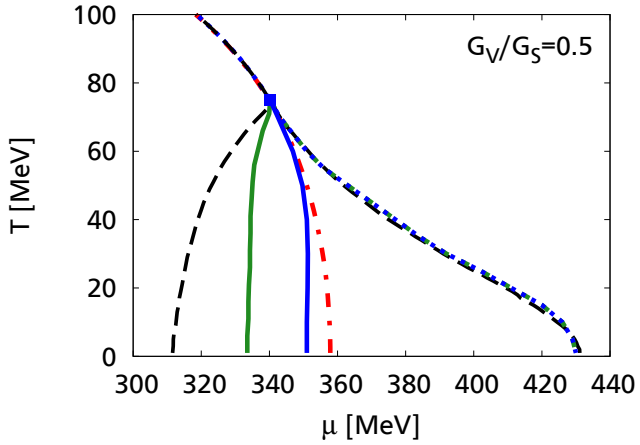

Figure 6.5.: Phase diagram with sinusoidal modulations with spatially-varying $\tilde{\mu}$ (blue, solid and dotted), homogeneous solutions (red, dashed dotted), chiral density wave (green, solid and dashed) and solitonic modulations with constant shifted chemical potentials (black, dashed). Solid lines indicate first-order phase transitions, all other line types second-order transitions. (Data with solitonic modulation is courtesy of Stefano Carignano)

7 Competition between Chiral Density Wave and Sinusoidal Modulations

In the previous chapter we have seen, that for a vector coupling constant of $G_V/G_S = 0.5$ the chiral density wave is favored over the sinusoidal modulation with spatially varied density. Since for vanishing vector coupling the sinusoidal modulations are favored and we expect the thermodynamic potential to be continuous in G_V, there should either be a critical coupling constant $G_{V,crit}$, where both modulations are degenerate with respect to their energies, or there should be a mixed inhomogeneous phase, with regions where the CDW is favored and regions where the sinusoidal modulation is favored. To find out which case is present here we compare the free energies at different vector coupling strengths in figure 7.1.

Similar to figure 6.4 we compare the free energies of both solutions with respect to the restored grand potential. For a weak vector coupling of $G_V/G_S = 0.1$ we find the sinusoidal modulation still to be favored, but the difference decreases for a larger coupling constant $G_V/G_S = 0.25$. Upon further increasing the strength of the vector interaction $G_V/G_S = 0.3$, we find a crossing in the free energies of the two modulations, meaning we have two different inhomogeneous phases. At lower chemical potentials the chiral density wave is favored and at a critical μ the sinusoidal modulation takes over. The two modulations seem to have the same transition to the restored phase, as we have already seen in the previous chapter. Further increasing the coupling constant $G_V/G_S = 0.4$ leads to the CDW being favored in the

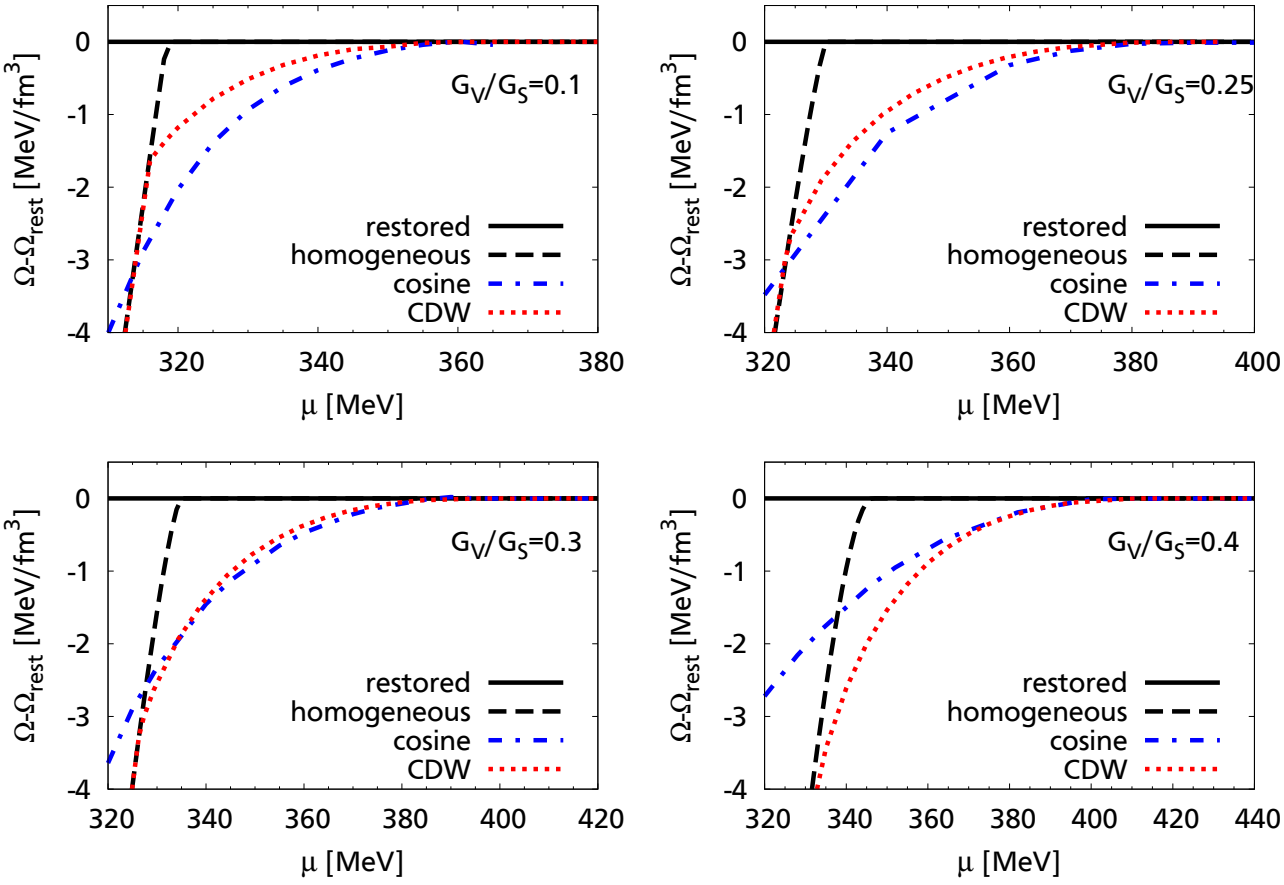

Figure 7.1.: Free energies of CDW and sinusoidal modulations for different vector-coupling strengths at $T = 1$ MeV.

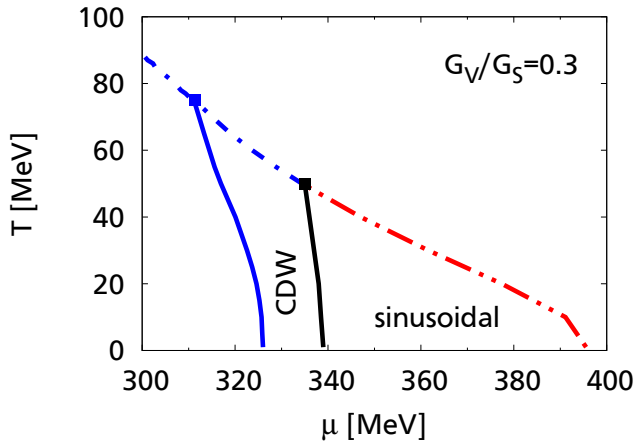

Figure 7.2.: Phase diagram with mixed inhomogeneous phase at $G_V/G_S = 0.3$. Blue lines (solid and dashed-dotted) indicate transitions of the CDW and homogeneous phases, the red line (double-dotted dashed) indicates the transition from the sinusoidal modulations to the restored phase and the black line indicates the transition from CDW to sinusoidal modulations. Solid lines are used for first-order transitions and dashed ones for second-order.

whole inhomogeneous phase.
The behavior for $G_V/G_S = 0.3$ is of particular interest, as both modulations seem to coexist. The phase diagram, figure 7.2, shows four different phases now, in addition to the homogeneous broken and the restored phase, we find a phase where the chiral density wave is favored for lower chemical potentials and a phase where the sinusoidal modulation is favored at higher μ. In addition the sinusoidal modulation only appears up to a temperature of about $T = 50$ MeV. The transition from the CDW to the cosine is of first order.
It would be interesting to see, whether this behavior is the same if we allowed more Fourier coefficients for the effective mass and the shifted chemical potential. Another possibility would be to go to an ansatz where the first and minus first Fourier coefficients are independent ($M_{-1} \neq M_1$), to see if the parameters adjust themselves self-consistently to a similar behavior. In this ansatz the effective mass could take the form of a chiral density wave as well as the form of a cosine and even a smooth transition is possible.
In the region close to the restored phase the energy differences become smaller, the two solutions approach each other here. We would expect the sinusoidal to remain favored and both solutions to become degenerate at the phase transition. Even for higher coupling strengths there might be a region where the cosine is favored. Our energy resolution is not precise enough to verify this, but a solution would be to investigate this with a Ginzburg-Landau expansion, see [30].

8 Conclusion and Outlook

In this thesis we investigated inhomogeneous chiral symmetry breaking phases with vector interactions in the Nambu–Jona-Lasinio model.
We introduced the Lagrangian of the NJL model with vector interactions and performed a mean-field approximation, allowing for periodic modulations in space. The case of homogeneous condensates was briefly discussed and some selected numerical results were given. We proceeded with some necessary preparations to calculate the thermodynamic potential of inhomogeneous condensates, where we discretized the Hamiltonian and applied a cutoff to render it finite and gave some results for the sinusoidal modulations with spatially-varying shifted chemical potentials, like the order parameter and the density as a function of the chemical potential and a phase diagram. We have found the inclusion of explicitly modulated densities to have a significant effect on the phase diagram. Compared to the case without vector interactions the inhomogeneous phase broadens to a wider chemical potential range, the phase transition from the homogeneous chirally broken to the restored phase is replaced by the inhomogeneous phase for temperatures below the critical temperature. The inhomogeneous condensates are favored up to a critical temperature, which coincides with the temperature of the critical point for the homogeneous case without vector interactions, where we find a Lifschitz point.
We compared our results to other modulations, where the shifted chemical potential had no explicit spatial variation and found some differences in the transition from the homogeneous broken to the inhomogeneous phase. Investigating the free energies of the modulations, we found the chiral density wave to be favored for higher vector coupling strengths. We could test our assumptions for the density wave number for the sinusoidal modulation.
When we analyzed the free energies of the sinusoidal modulations and the chiral density wave, we found that the sinusoidal modulation is favored for lower vector couplings, before at $G_V/G_S \approx 0.3$ we find that both modulations start to compete and we have a mixed inhomogeneous phase.

Outlook

We already know, that the sinusoidal modulations are not the favored solution at vanishing vector coupling and don't expect them to be when vector interactions are enabled. It would be interesting to see if other modulations, with more Fourier components would deliver energetically favored results. Since the solitonic modulations are favored in the case without vector interactions, it might be interesting to implement those for the case with explicit modulations of the density. While analytic solutions like in section 6.1 are not known, one can implement this case with the Fourier decomposition of $M(z) = M\mathrm{sn}(z|\nu)$ for a finite number of coefficients. It would be interesting to see, whether the chiral density wave would still be favored at higher coupling constants. The problem is, that taking more Fourier components leads to Hamiltonians with more off-diagonal elements, which slows down the calculations extremely.
The competition between the chiral density wave and the sinusoidal modulation needs some further treatment. Calculations at different coupling strengths and detailed view at the behavior close to the restored phase should be done. In this regime the resolution of our calculations is not sufficient, but the problem could be treated by utilizing a Ginzburg-Landau expansion.

A Spatial Vector Condensate in Direction of the Modulation

Like we already mentioned in chapter 2, restricting ourselves only to the zero component of the vector interaction, namely the density, might be questionable for one-dimensional modulations. We already broke the rotational symmetry by allowing modulations of the order parameter in the z-direction only. In this case one could expect the 3-component of the vector interaction to contribute. In this section we want to show that a vanishing spatial condensate in the direction of the modulation still leads to a self-consistent solution.
First of all take the Lagrangian again

$$\mathscr{L} = \overline{\psi}\left(i\partial\!\!\!/\right)\psi + G_S\left[\left(\overline{\psi}\psi\right)^2 + \left(\overline{\psi}\gamma_5\tau^a\psi\right)^2\right] - G_V\left[\left(\psi^\dagger\psi\right)^2 - \left(\overline{\psi}\gamma^k\psi\right)^2\right]. \tag{A.1}$$

This is only another way of writing the Lagrangian in the chiral limit, but it already shows, that the spatial components of the vector interaction can be expected to be attractive. We perform a mean-field approximation as before, only this time allowing for an additional condensate

$$\left(\overline{\psi}\gamma^3\psi\right)^2 \approx -n_3^2(z) + 2n_3(z)\overline{\psi}\gamma^3\psi, \tag{A.2}$$

where we restricted ourselves to a one-dimensional modulation in z direction. Most steps here work analogously to chapter 2.
We define, similar to $M(z)$ and $\tilde{\mu}(z)$,

$$\eta(z) = -2G_V n_3(z) \tag{A.3}$$

and arrive at the mean-field Lagrangian

$$\mathscr{L}_{MF} = \overline{\psi}\left(i\partial\!\!\!/ - M(z) - \gamma^3\eta(z)\right)\psi + (\tilde{\mu}(z) - \mu)\psi^\dagger\psi - \mathscr{V}, \tag{A.4}$$

$$-\mathscr{V} = -\frac{|M(z)|^2}{4G_S} - \frac{\eta^2(z)}{4G_V} + \frac{(\tilde{\mu}(z)-\mu)^2}{4G_V}. \tag{A.5}$$

The effective Hamiltonian in coordinate space is

$$\mathscr{H} - \mu\psi^\dagger\psi = \begin{pmatrix} i\vec{\sigma}\vec{\partial} - \tilde{\mu}(z) + \sigma_3\eta(z) & M(z) \\ M^*(z) & -i\vec{\sigma}\vec{\partial} - \tilde{\mu}(z) - \sigma_3\eta(z) \end{pmatrix}. \tag{A.6}$$

We can show, that a vanishing η condensate is a self-consistent solution. To do this we prove that $\Omega(\eta) = \Omega(-\eta)$ holds. We go to the Hamiltonian in momentum space and focus on the Dirac structure

$$\mathscr{H}(+\eta) = \begin{pmatrix} p_z + \eta(p_z) - \tilde{\mu}(p_z) & -p_\perp & M(p_z) & 0 \\ -p_\perp & -p_z - \eta(p_z) - \tilde{\mu}(p_z) & 0 & M(p_z) \\ M(p_z) & 0 & -p_z - \eta(p_z) - \tilde{\mu}(p_z) & p_\perp \\ 0 & M(p_z) & p_\perp & p_z + \eta(p_z) - \tilde{\mu}(p_z) \end{pmatrix}. \tag{A.7}$$

We apply a similarity transformation

$$U = \begin{pmatrix} 0 & 1 & 0 & 0 \\ 1 & 0 & 0 & 0 \\ 0 & 0 & 0 & 1 \\ 0 & 0 & 1 & 0 \end{pmatrix}, \tag{A.8}$$

which does not change the eigenvalues. The resulting matrix has just a change in the signs of p_z and $\eta(p_z)$

$$U^{-1}\mathscr{H}(+\eta)U = \begin{pmatrix} -p_z - \eta(p_z) - \tilde{\mu}(p_z) & -p_\perp & M(p_z) & 0 \\ -p_\perp & p_z + \eta(p_z) - \tilde{\mu}(p_z) & 0 & M(p_z) \\ M(p_z) & 0 & p_z + \eta(p_z) - \tilde{\mu}(p_z) & p_\perp \\ 0 & M(p_z) & p_\perp & -p_z - \eta(p_z) - \tilde{\mu}(p_z) \end{pmatrix}. \tag{A.9}$$

To get the thermodynamic potential we have to integrate over p_z from $-\infty$ to ∞, so we can substitute $p_z \to -p_z$ without altering the overall potential. The condensates for our case are symmetric with respect to p_z anyway, as they only depend on the size of the Brillouin zone and not on the overall momentum. The resulting Hamiltonian

$$\begin{aligned} U^{-1}\mathscr{H}(+\eta)U &= \begin{pmatrix} p_z - \eta(p_z) - \tilde{\mu}(p_z) & -p_\perp & M(p_z) & 0 \\ -p_\perp & -p_z + \eta(p_z) - \tilde{\mu}(p_z) & 0 & M(p_z) \\ M(p_z) & 0 & -p_z + \eta(p_z) - \tilde{\mu}(p_z) & p_\perp \\ 0 & M(p_z) & p_\perp & p_z - \eta(p_z) - \tilde{\mu}(p_z) \end{pmatrix} \\ &= \mathscr{H}(-\eta) \end{aligned} \tag{A.10}$$

equals the one with a negative sign for η, but gives the same value for the thermodynamic potential.
So $\Omega(\eta) = \Omega(-\eta)$ for all values of η, so $\eta = 0$ must be an extremum of the thermodynamic potential and is a self-consistent solution.
Furthermore, we have not found additional solutions for η in numerical calculations. All test cases have shown, that $\eta = 0$ is the only solution.

B Necessity of the Sign Function

In chapter 4 we introduced the sign function in the thermodynamic potential when we regularized the energy eigenvalues. To see that this is a necessary procedure we look at the limit of pairwise occurring eigenvalues of the Hamiltonian.
First of all we would like to state, that the introduction of the sign function does not change the grand potential, since the hyperbolic cosine is symmetric around zero

$$\sum_{E_\lambda} T \ln\left[2\cosh\left(\frac{E_\lambda-\tilde{\mu}_0}{2T}\right)\right] = \sum_{E_\lambda} T \ln\left[2\cosh\left(\frac{\mathrm{sgn}(E_\lambda)(E_\lambda-\tilde{\mu}_0)}{2T}\right)\right]. \tag{B.1}$$

If we regularize this term, in the limit of pairwise occurring eigenvalues $\{E_\lambda, -E_\lambda\}$ we should end up with

$$\sum_{E_\lambda>0}\sum_{j=0}^{3} c_j \left[E_{\lambda,j} + T\ln\left(1+\exp\left(-\frac{E_{\lambda,j}-\tilde{\mu}_0}{T}\right)\right) + T\ln\left(1+\exp\left(-\frac{E_{\lambda,j}+\tilde{\mu}_0}{T}\right)\right)\right]. \tag{B.2}$$

In fact, if we try to regularize the cosh without the sign function we cannot reproduce this limit

$$\sum_{E_\lambda}\sum_{j=0}^{3} c_j T \ln\left[2\cosh\left(\frac{E_{\lambda,j}-\tilde{\mu}_0}{2T}\right)\right] \tag{B.3}$$

$$= \sum_{E_\lambda>0}\sum_{j=0}^{3} c_j 2T \ln\left[2\cosh\left(\frac{E_{\lambda,j}-\tilde{\mu}_0}{2T}\right)\right] \tag{B.4}$$

$$= \sum_{E_\lambda>0}\sum_{j=0}^{3} c_j \left(E_{\lambda,j}-\tilde{\mu}_0 + 2T\ln\left[1+\exp\left(-\frac{E_{\lambda,j}-\tilde{\mu}_0}{T}\right)\right]\right). \tag{B.5}$$

If we use the sign function instead, the limit is easily reproducible

$$\sum_{E_\lambda}\sum_{j=0}^{3} c_j T \ln\left[2\cosh\left(\frac{E_{\lambda,j}-\mathrm{sgn}(E_\lambda)\tilde{\mu}_0}{2T}\right)\right] \tag{B.6}$$

$$= \sum_{E_\lambda>0}\sum_{j=0}^{3} c_j T \ln\left[2\cosh\left(\frac{E_{\lambda,j}-\tilde{\mu}_0}{2T}\right)\right] + T\ln\left[2\cosh\left(\frac{E_{\lambda,j}+\tilde{\mu}_0}{2T}\right)\right] \tag{B.7}$$

$$= \sum_{E_\lambda>0}\sum_{j=0}^{3} c_j \left[\frac{E_{\lambda,j}-\tilde{\mu}_0}{2} + T\ln\left[1+\exp\left(-\frac{E_{\lambda,j}-\tilde{\mu}_0}{T}\right)\right]\right. \tag{B.8}$$

$$\left. + \frac{E_{\lambda,j}+\tilde{\mu}_0}{2} + T\ln\left[1+\exp\left(-\frac{E_{\lambda,j}+\tilde{\mu}_0}{T}\right)\right]\right]$$

$$= \sum_{E_\lambda>0}\sum_{j=0}^{3} c_j \left[E_{\lambda,j} + T\ln\left(1+\exp\left(-\frac{E_{\lambda,j}-\tilde{\mu}_0}{T}\right)\right) + T\ln\left(1+\exp\left(-\frac{E_{\lambda,j}+\tilde{\mu}_0}{T}\right)\right)\right]. \tag{B.9}$$

This shows, that the sign function is needed in order to be consistent with the known limits.

C Asymptotic Eigenvalues

The most time demanding part in the calculations is to diagonalize the Hamiltonian. We always get cut-off artifacts and the only solution seems to be to apply a very large cutoff, typically around 8 to 10 GeV. In order to choose smaller cutoffs and reach a higher precision in our calculations, we want to investigate the behavior of the eigenvalues for very large momenta, both in the direction parallel to the modulation and perpendicular to it. We expect $(k - mq)$ and $p_\perp$ to be very large compared to M_1 and $\tilde{\mu}_1$.
In order to get the asymptotic behavior of the eigenvalues we use standard quantum mechanics perturbation methods, that can be found for example in [31]. We divide the Hamiltonian into two parts, the unperturbed H_0 and the perturbation H_1

$$\left(H_0\right)_{p,p'} = \gamma_0\gamma_3(k - nq)\delta_{p,p'} + \gamma_0\gamma_1 p_\perp \delta_{p,p'} + \gamma_0 M_0 \delta_{p,p'}, \tag{C.1}$$

$$\left(H_1\right)_{p,p'} = \gamma_0 \frac{M_1}{2}\delta_{p-q,p'} + \gamma_0 \frac{M_1}{2}\delta_{p,p'-q} - \frac{\tilde{\mu}_1}{2}\delta_{p-2q,p'} - \frac{\tilde{\mu}_1}{2}\delta_{p,p'-2q}. \tag{C.2}$$

We see immediately that H_0 is diagonal in momentum space and we can calculate the eigenvalues analytically

$$E_n^{(0)} = \pm\sqrt{p_\perp^2 + (k - nq)^2 + M_0^2}. \tag{C.3}$$

The corresponding eigenvectors $w_m^{(0)}$ of H_0 follow the relation

$$w_m^{(0)^\dagger} w_n^{(0)} = \delta_{n,m}, \tag{C.4}$$

which means they are non-vanishing only if $p = p'$, so it is clear that the first-order perturbation vanishes

$$E_n^{(1)} = w_n^{(0)^\dagger} H_1 w_n^{(0)} = 0, \tag{C.5}$$

as H_1 only got off diagonal entries in momentum space. The second-order perturbation looks the following

$$E_n^{(2)} = \sum_{m\neq n} \frac{|w_m^{(0)^\dagger} H_1 w_n^{(0)}|^2}{E_n^{(0)} - E_m^{(0)}}. \tag{C.6}$$

We only get a contribution if the momenta differ by a factor of one or two q, so we do not need to care about the degeneracy of the unperturbed eigenvalues. We obtain

$$E_n^{(2)} = \sum_{m\neq n} \frac{|M_1/2\ \delta_{m,n\pm1} - \tilde{\mu}_1/2\ \delta_{m,n\pm2}|^2}{E_n^{(0)} - E_m^{(0)}}. \tag{C.7}$$

Due to the Kronecker delta there are no mixed terms from the square in (C.7) and the second-order energy correction reads

$$E_n^{(2)} = \frac{M_1^2}{4\left(E_n^{(0)} - E_{n+1}^{(0)}\right)} + \frac{M_1^2}{4\left(E_n^{(0)} - E_{n-1}^{(0)}\right)} + \frac{\tilde{\mu}_1^2}{4\left(E_n^{(0)} - E_{n+2}^{(0)}\right)} + \frac{\tilde{\mu}_1^2}{4\left(E_n^{(0)} - E_{n-2}^{(0)}\right)}. \tag{C.8}$$

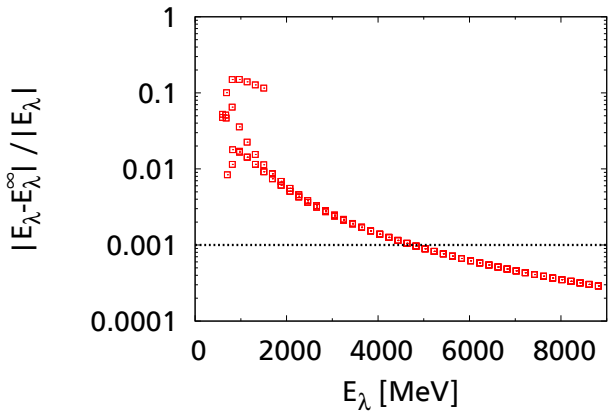

Figure C.1.: Relative difference between the exact eigenvalues of $\mathscr{H}$ and the energies from the perturbation ansatz for examplary values $k = 200$ MeV, $q = 200$ MeV, $p_\perp = 500$ MeV, $M_0 = 0$ MeV, $M_1 = 300$ MeV and $\tilde{\mu}_1 = 100$ MeV. The matrix cutoff for $\mathscr{H}$ is $\Lambda_M = 10$ GeV.

The energy correction up to second order is

$$E_\lambda^\infty := E_\lambda^{(0)} + E_\lambda^{(2)}, \tag{C.9}$$

where, due to the degeneracy in Dirac space, we get each energy two times. To find a feasible cutoff for our matrix we compare the asymptotic eigenvalues to the exact ones using a large matrix cutoff Λ_M. In figure C.1 the relative difference $|E_\lambda - E_\lambda^\infty|/|E_\lambda|$ is plotted against the energy E_λ. A reasonable large cutoff Λ_M is used, so that the eigenvalues E_λ can be considered exact in the range shown in the figure. We see, that for the given values the relative difference drops under 1 per mill at an energy of approximately 5 GeV. This is true for all tested cases, so we will cut the matrix at $\Lambda_M = 5$ GeV and use the asymptotic eigenvalues for higher energies.
This formalism can easily be applied to the thermodynamic potential (4.18) and to the self-consistent equation for $\tilde{\mu}_0$ (4.31). To use the asymptotic eigenvalues for (4.33) we just take the derivative of the perturbed eigenvalues

$$\frac{\partial E_\lambda^\infty}{\partial \tilde{\mu}_1} = \frac{\tilde{\mu}_1}{2\left(E_n^{(0)} - E_{n+2}^{(0)}\right)} + \frac{\tilde{\mu}_1}{2\left(E_n^{(0)} - E_{n-2}^{(0)}\right)}. \tag{C.10}$$

D Finding Self-Consistent Parameters

For the sinusoidal modulation we have to determine a set of four self-consistent parameters: the mass amplitude M, the wave number q and the two Fourier components of the shifted chemical potential $\tilde{\mu}_0$ and $\tilde{\mu}_1$. The major problem doing this is numerical precision. The gap equations for M and $\tilde{\mu}_1$ demand calculating the normalized eigenvectors and include the modified scalar product from the derivative of the eigenvalues $w_\lambda^\dagger(\partial\mathscr{H}/\partial x)w_\lambda$. Calculating the eigenvectors significantly slows down the overall process and a very high precision is needed to achieve useful results from the modified scalar product. In addition, for large matrices, we have large eigenvectors and have to sum over a list of very small numbers, which is a potential source of rounding errors.
Instead of doing the exact calculations for the gap equations, one could naively try to use a difference quotient and calculate it numerically

$$\frac{\partial\Omega(x)}{\partial x} = \frac{\Omega(x+\Delta x)-\Omega(x-\Delta x)}{2\Delta x} \stackrel{!}{=} 0.$$

The problem doing this is again numerical precision. If we use the difference quotient we have a strong dependency on the accuracy of the thermodynamic potential. The ratio between the the gap equation and the thermodynamic potential is about 10^{-6}, so to get a useful gap equation we need to achieve a relative error of 10^{-8} in the grand potential. This however is not a feasible way, calculating to this precision would take too long. Another possible way would be to calculate the potential at more supporting points, giving a statistically better result, but this again takes an enormous amount of time. It is in most cases possible, to get an idea of the behavior of the gap equations, but the relatively large errors make it very difficult to find their roots numerically. In the Newton method for example the error in the gap equations would result in an even larger error in the Jacobi matrix, so we can not expect convergence.
What we need is an algorithm that is stable against smaller errors in the thermodynamic potential. In the case without vector interactions in most cases a minimization algorithm is used, refer to [32], which minimizes the thermodynamic potential. In the minima of the potential, the gap equations are fulfilled. This is not possible in our case, since the vector channel contributions maximize the grand potential. Instead we introduce a different formalism.
One way to get a function that we can calculate numerically is fitting a polynomial to the grand potential. The least sums of squares fit does not have a great dependence on small errors in the potential. In addition, at least for the sinusoidal case, the functions are very well behaving and can be very good approximated with polynomials. With a reasonable number of supporting points, we can find good solutions. We can use properties of the problem, like the symmetry of the mass $\Omega(M) = \Omega(-M)$ to further increase the precision. In practice we found that polynomials up to fifth order (sixth for the mass amplitude) are sufficient, to deliver good results:

$$\Omega_{fit}(M,q,\tilde{\mu}_0,\tilde{\mu}_1) = \left(\sum_{i=0}^{3} a_{2i}M^{2i}\right)\left(\sum_{j=0}^{5} b_j q^j\right)\left(\sum_{k=0}^{5} c_k\tilde{\mu}_0^k\right)\left(\sum_{l=0}^{5} d_l\tilde{\mu}_1^l\right). \tag{D.1}$$

Here we already used the symmetry of the mass amplitude.
To validate our results we check the results obtained from the fitted function against the numerical gap equations, using the difference quotient with multiple supporting points as described above.

Bibliography

[1] M. Gell-Mann, "A Schematic model of baryons and mesons," *Phys. Lett.* **8** (1964) 214–215.

[2] H. Fritzsch, M. Gell-Mann, and H. Leutwyler, "Advantages of the Color Octet Gluon Picture," *Phys.Lett.* **B47** (1973) 365–368.

[3] F. Karsch, "Lattice QCD at high temperature and density," *Lect.Notes Phys.* **583** (2002) 209–249, arXiv:hep-lat/0106019 [hep-lat].

[4] C. Allton, S. Ejiri, S. Hands, O. Kaczmarek, F. Karsch, *et al.*, "The Equation of state for two flavor QCD at nonzero chemical potential," *Phys.Rev.* **D68** (2003) 014507, arXiv:hep-lat/0305007 [hep-lat].

[5] P. Braun-Munzinger and J. Wambach, "The Phase Diagram of Strongly-Interacting Matter," *Rev.Mod.Phys.* (2008) , arXiv:0801.4256 [hep-ph].

[6] K. Fukushima and T. Hatsuda, "The phase diagram of dense QCD," *Rept.Prog.Phys.* **74** (2011) 014001, arXiv:1005.4814 [hep-ph].

[7] F. J. Dyson, "The S Matrix in Quantum Electrodynamics," *Phys. Rev.* **75** (Jun, 1949) 1736–1755. http://link.aps.org/doi/10.1103/PhysRev.75.1736.

[8] J. Schwinger, "On the Green's functions of quantized fields. I," *Proceedings of the National Academy of Sciences* **37** no. 7, (1951) 452–455.

[9] J. Schwinger, "On the Green's functions of quantized fields. II," *Proceedings of the National Academy of Sciences* **37** no. 7, (1951) 455–459.

[10] Y. Nambu and G. Jona-Lasinio, "Dynamical Model of Elementary Particles Based on an Analogy with Superconductivity. I," *Phys. Rev.* **122** (Apr, 1961) 345–358. http://link.aps.org/doi/10.1103/PhysRev.122.345.

[11] Y. Nambu and G. Jona-Lasinio, "Dynamical Model of Elementary Particles Based on an Analogy with Superconductivity. II," *Phys. Rev.* **124** (Oct, 1961) 246–254. http://link.aps.org/doi/10.1103/PhysRev.124.246.

[12] M. Buballa, "NJL model analysis of quark matter at large density," *Phys.Rept.* **407** (2005) 205–376, arXiv:hep-ph/0402234 [hep-ph].

[13] J. Walecka, "A theory of highly condensed matter," *Annals of Physics* **83** no. 2, (1974) 491 – 529. http://www.sciencedirect.com/science/article/pii/0003491674902085.

[14] C. Christov, K. Goeke, and M. V. Polyakov, "NJL model with vector couplings versus phenomenology," arXiv:hep-ph/9501383 [hep-ph].

[15] A. W. Overhauser, "Structure of Nuclear Matter," *Phys. Rev. Lett.* **4** (Apr, 1960) 415–418. http://link.aps.org/doi/10.1103/PhysRevLett.4.415.

[16] P. Fulde and R. A. Ferrell, "Superconductivity in a Strong Spin-Exchange Field," *Phys. Rev.* **135** (Aug, 1964) A550–A563. http://link.aps.org/doi/10.1103/PhysRev.135.A550.

[17] A. Larkin and Y. Ovchinnikov, "Nonuniform state of superconductors," *Zh.Eksp.Teor.Fiz.* **47** (1964) 1136–1146.

[18] D. J. Gross and A. Neveu, "Dynamical symmetry breaking in asymptotically free field theories," *Phys. Rev. D* **10** (Nov, 1974) 3235–3253. http://link.aps.org/doi/10.1103/PhysRevD.10.3235.

[19] V. Schön and M. Thies, "Emergence of the Skyrme crystal in Gross-Neveu and 't Hooft models at finite density," *Phys. Rev. D* **62** (Sep, 2000) 096002. http://link.aps.org/doi/10.1103/PhysRevD.62.096002.

[20] O. Schnetz, M. Thies, and K. Urlichs, "Phase diagram of the Gross-Neveu model: Exact results and condensed matter precursors," *Annals Phys.* **314** (2004) 425–447, arXiv:hep-th/0402014 [hep-th].

[21] O. Schnetz, M. Thies, and K. Urlichs, "Full phase diagram of the massive Gross-Neveu model," *Annals Phys.* **321** (2006) 2604–2637, arXiv:hep-th/0511206.

[22] D. Nickel, "Inhomogeneous phases in the Nambu-Jona-Lasino and quark- meson model," *Phys. Rev.* **D80** (2009) 074025, arXiv:0906.5295 [hep-ph].

[23] M. Buballa and D. Nickel, "Inhomogeneous phases of strongly interacting matter," *Acta Phys.Polon.Supp.* **3** (2010) 523–532, arXiv:0911.2333 [hep-ph].

[24] S. Carignano, D. Nickel, and M. Buballa, "Influence of vector interaction and Polyakov loop dynamics on inhomogeneous chiral symmetry breaking phases," *Phys. Rev.* **D82** (2010) 054009, arXiv:1007.1397 [hep-ph].

[25] J. Kapusta, *Finite Temperature Field Theory*. Cambridge University Press, 2005.

[26] S. Klevansky, "The Nambu-Jona-Lasinio model of quantum chromodynamics," *Rev.Mod.Phys.* **64** (1992) 649–708.

[27] W. Pauli and F. Villars, "On the Invariant Regularization in Relativistic Quantum Theory," *Rev. Mod. Phys.* **21** (Jul, 1949) 434–444. http://link.aps.org/doi/10.1103/RevModPhys.21.434.

[28] J. Gasser and H. Leutwyler, "Low energy theorems as precision tests of QCD," *Physics Letters B* **125** no. 4, (1983) 325 – 329. http://www.sciencedirect.com/science/article/pii/0370269383912947.

[29] D. Nickel and M. Buballa, "Solitonic ground states in (color-) superconductivity," *Phys.Rev.* **D79** (2009) 054009, arXiv:0811.2400 [hep-ph].

[30] D. Nickel, "How many phases meet at the chiral critical point?," *Phys.Rev.Lett.* **103** (2009) 072301, arXiv:0902.1778 [hep-ph].

[31] J. J. Sakurai, *Modern Quantum Mechanics*. Pearson Education Inc., 1994.

[32] J. A. Nelder and R. Mead, "A Simplex Method for Function Minimization," *Computer Journal* **7** (1965) 308–313.